Development of Mechanically Reinforced Free-standing Nanomembranes

アンテネ, キンドゥ, メルシャ

Development of Mechanically Reinforced Free-standing Nanomembranes

Anteneh Kindu Mersha

Department of Chemistry and Biochemistry

Graduate School of Engineering

KYUSHU UNIVERSITY

2019

Table of contents

Chapter 1 General Introduction

1.1 Free-standing nanomembranes

Following the Richard Feynman's 1959 lecture 'There's Plenty of Room at the Bottom', which challenged the science community to think small, the field of nanotechnology is now maturing rapidly with the fabrication of unique or enhanced materials, products and devices.[1,2]

Nanomembranes are important class of nanotechnology, with significantly advancing applications in a wide range of areas including molecular separations,[3–6] energy conversion and storage,[7–10] sensing,[11,12] catalysis[13] and biomedical applications,[12,14] owing to their nanometer thickness and large lateral dimensions. A nanomembrane comprise thicknesses of less than a few hundred nanometers and minimum lateral dimensions of at least two orders of magnitude larger than the thickness.[7,12] Free-standing nanomembranes (FS-NMs) are defined as self-supporting nanomembranes with dual surfaces that can physically separate two spaces,[15,16] by sustaining their size and shape without support.[17,18]

FS-NMs offer unique advantages that are difficult (or otherwise impossible) to achieve using their bulk analogues and other material forms because of the following features. (i) despite their nano-thickness, FS-NMs can be transferred onto any arbitrary substrate of diverse configurations such as planar, curvilinear or wavy structures.[7,12,19] Such properties allow the design of devices which cannot be achieved with conventional technologies that rely on rigid, planar materials. For example, a human eye-inspired hemispherical imaging devices present practical routes for integrating well-developed planar device technologies (such as semiconductor wafers) onto the surfaces of complex curvilinear objects.[20] (ii) They have high size to thickness aspect ratio of greater than 10^6.[15] (iii) FS-NMs have unique interfacial and mechanical properties, including noncovalent adhesiveness, flexibility and high molecular flux for separation.[15,21] (iv) They also provide opportunities for dual surface functionalization in applications such as solid-electrolytes for batteries.

1.2 Fabrication of freestanding nanomembranes

Preparation of nanomembranes with self-supporting nature is not an easy task since it requires careful release and handling of the nanomembrane from the substrate without damage. There are two methods to fabricate FS-NMs; sacrificial layer and support layer approaches, as illustrated in Figure 1-1. In the sacrificial layer approach, two possible substrates can be employed; A polymer

pre-coated on a solid substrate such as glass (Figure 1-1a) that can be dissolved in a particular solvent or a silicon wafer which can be etched by strong acid or alkaline solution (Figure 1-1b).

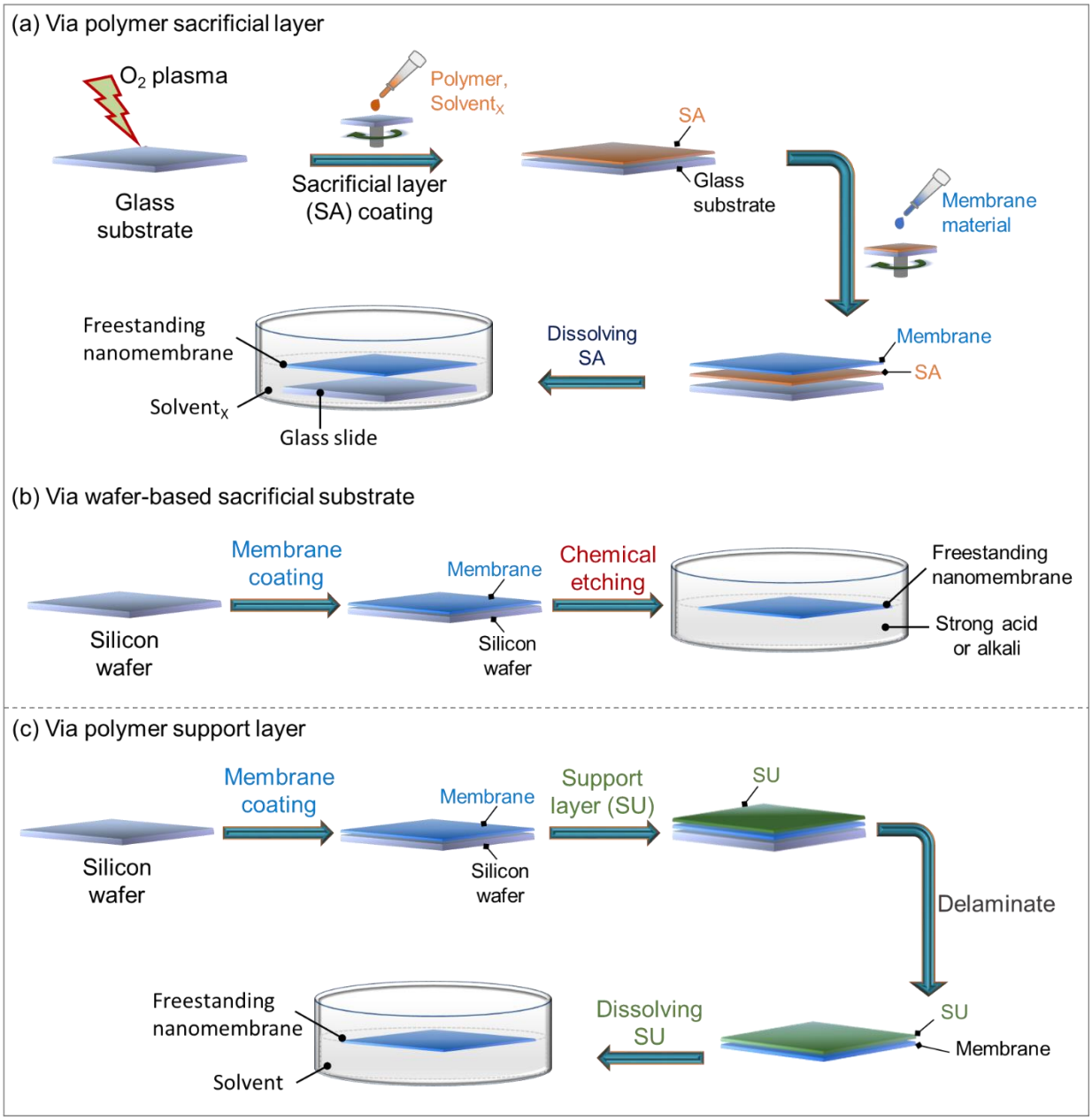

Figure 1-1. Schematic illustration of FS-NM preparation procedures. (a) Via polymer sacrificial layer: it is a commonly used approach, and applicable to the majority of nanomembrane deposition techniques. (b) Via wafer-based sacrificial substrate: it is generally used for the preparation of polymeric FS-NMs which are stable in strong acid/alkaline solution. (c) Via polymer support layer: it is often utilized in the fabrication of metallic and metal oxide FS-NMs. In the current study, polymer sacrificial layer approach using poly(4-vinyl phenol) was employed.

In either case, the nanomembrane material is deposited on the sacrificial layer by various techniques such as spin coating, dip coating, spray coating, spin/dip/spray-assisted layer-by-layer assembly,[22] Langmuir–Blodgett,[23] as well as chemical and physical vapor depositions. Spin-coating is a versatile method to prepare ultrathin membranes as it allows the deposition of highly ordered nanostructures with prediction and control of precise film thickness and surface roughness.[24]

Once the nanomembrane is prepared, the sacrificial layer is selectively removed by dissolution or chemical etching, releasing the self-supporting nanomembrane (Figure 1-1a, b). There is no special requirement for a sacrificial layer material, however, it should have smooth surface and should be readily soluble in a particular solvent.

In the case of support layer approach (Figure 1-1c), the nanomembrane material is first coated on a solid substrate followed by thick supporting layer. Afterwards, the weakly adhered nanomembrane is peeled off from the solid substrate together with the support. Eventually, the support layer is removed by selective dissolution in a suitable solvent, which releases the FS-NM floating on the surface.

At this stage, the nanomembrane could be ready for the desired function. It can be transferred onto other substrates while in the detachment solvent or it can be lifted off and mounted onto a preferred surface for use.

1.3 Challenges in developing functional freestanding nanomembranes

To be used for a specific purpose, nanomembranes should satisfy some essential requirements; self-supporting nature, mechanical strength and defect or crack freeness (Figure 1-2). The merits of nano-scale thickness and free-standing nature have been explained in the previous section. The need for mechanical strength in nanomembranes and enhancement methods are discussed in the following section. Along with mechanical robustness is prevention of defects that can possibly be generated either during the film preparation step or during processing steps such as detachment, transfer onto other substrates and usage-related stress.

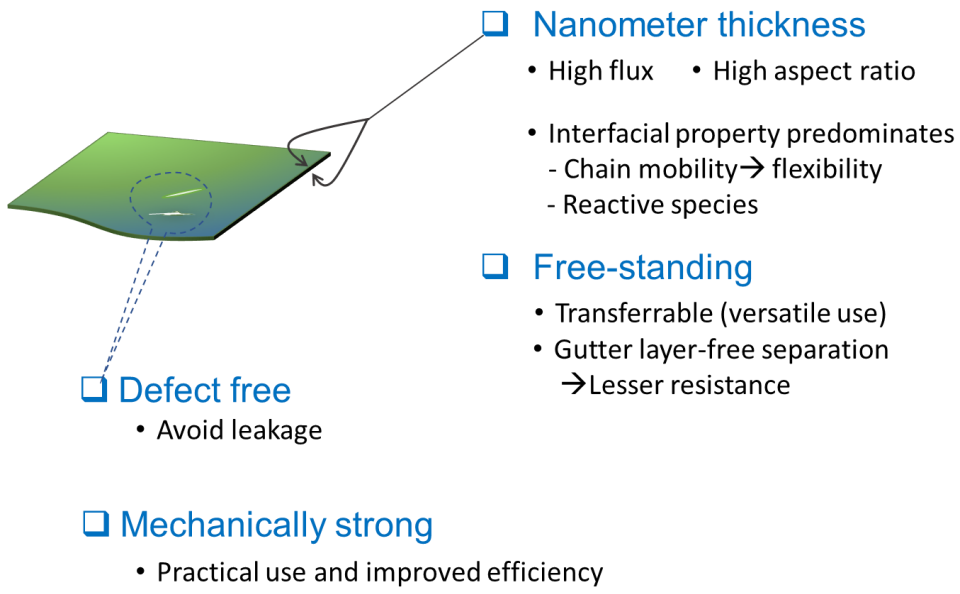

Figure 1-2. Required parameters in designing FS-NMs.

1.4 Mechanical enhancement in nanomembranes

The fabrication of nanomembranes for diverse applications is an established technology. However, only little effort has been put to resolve their mechanical property issues. To fully utilize the appealing features of FS-NMs in a wide range of applications, they need to have sufficient mechanical and chemical stabilities in the macroscopic scale. For example, due to their ultrathinness, FS-NMs are expected to enhance mass transport with less energy in separation applications. However, membrane thinning is often encountered by mechanical weakening.[25] Also, excellent mechanical stability of FS-NMs is highly desired in practical applications such as wound-dressing, antibacterial therapeutics and cellular organization scaffolding,[12] where FS-NMs are installed onto uneven surfaces.

Therefore, macroscopic mechanical reinforcement is a critical research challenge in the development of FS-NMs. Generally, the mechanical property problem in nanomembranes is originated from the inherent properties of materials, meaning that polymers are too soft[25] and inorganic materials are too fragile.[26] Thus, combining these two materials has been considered as a straightforward approach to develop composite materials with synergetic mechanical enhancement. Some of the strategies are discussed in the following sub-sections.

1.4.1 Nanoparticle filler approach

Incorporation of inorganic fillers into a polymer matrix[27–30] is a conventional approach for the preparation of mechanically reinforced organic/inorganic composite materials. Thus, nanocomposite membranes are consisted of micro- or nanoscale inorganic particles as the discrete phase and a polymeric material as a continuous or matrix phase[31] (Figure 1-3). Rigid nanoparticles such as metals,[28] metal oxides,[31] zeolites,[32] nanofibers such as carbon nanotubes (CNTs)[33] and nanosheets such as graphene[34] are frequently used fillers.

One dimensional materials such as CNTs[33,35,36] and metal oxide-based aluminosilicate naotubes (ASNTs),[37,38] are interesting class of reinforcements with high aspect ratio. They can form networked structures in a membrane that can act as a framework to anchor soft organic polymers. Such continuous fiber structures also resist crack propagation in ultrathin films.[39,40]

The mechanical properties of filler-reinforced membranes generally increase with increasing nanofiller loading at low volume fractions but then decrease at higher filler fractions due to issues related to agglomeration.[34] Large fillers and agglomerations flaw surface of the nanomembranes. This, in turn, strains stress movement (Figure 1-3), and eventually decreases tensile strength.

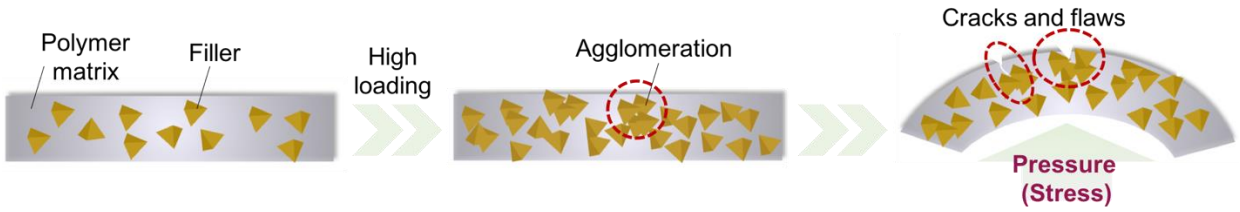

Figure 1-3. Schematic representation of inorganic fillers in a polymer matrix, and effect of agglomerations in mechanical properties.

1.4.2 Molecular level approaches

In the case of molecular level designs such as organic/inorganic interpenetrating networks,[41] crosslinked hard polymers[42] and layer-by-layer assembly,[18,22] the membrane materials are allowed to interact at the molecular or atomic scale. Such molecular level integration facilitates the development of ultrathin yet mechanically enhanced FS-NMs. These procedures often require materials to satisfy both the properties of membrane formation ability and functional moieties in a membrane form, limiting the range of material selection.

1.5 Motivation and summary of the thesis

Self-supporting nanomembranes are no longer theoretical and experimental curiosity, and are recognized as efficient nanomaterials for various applications, including membrane separations, electrolytes in energy storage and conversion, sensors and scaffolds for cellular and nanoparticle organization. However, attempts to develop highly compliant FS-NMs with unprecedented macroscopic mechanical stabilities remained a research challenge. Thus, the aim of the present dissertation is to address the toughing of FS-NMs which is essential for practical applications.

In the course of this research, an effort has been put to develop a facile strategy for the preparation of free-standing and mechanically strong, yet functional nanomembranes. Organic/inorganic composite materials are the subject of this research as they pave the way to synergetic mechanical reinforcement by combining the flexibility of polymers and rigidity of inorganics. The developed nanomembranes were tested for gas separation, which is among the most complex molecular separation processes due to its hypersensitivity to leakage. The main achievements of the research work are outlined as follows.

Firstly, a general introduction has been presented (**Chapter 1**) on the emergence of nanotechnology, the properties and advantages of nanomembranes, requirements to nanomembrane development, as well as mechanical enhancement strategies.

In **Chapter 2**, a sol-gel induced LBL assembly of metal oxide/polymer composite nanomembrane (Figure 1-4) is discussed. The spin-assisted LBL assembly of poly(vinyl alcohol) (PVA) and TiO_2 was aimed to maximize the synergetic mechanical enhancement between the polymer and metal oxide via strong sol-gel reactions. Accordingly, a few tenths nm thick, large size, highly flexible and free-standing nanomembrane was developed.

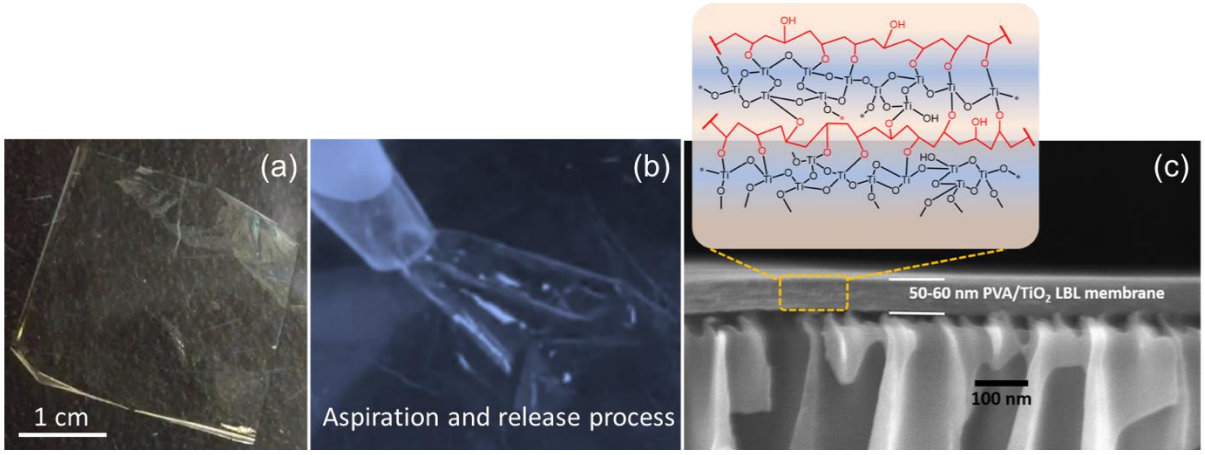

Figure 1-4. PVA/TiO_2 layer-by-layer nanomembrane. (a) Digital image of large-size, ca. 10 cm^2, nanomembrane floating on ethanol. (b) Aspiration and release process into a 2 mm diameter micropipette; the membrane retained its shape and size after the process. (c) SEM image of the nanomembrane transferred onto a porous support, *Inset:* Schematic illustration of the vertical membrane structure.

However, the membrane demonstrated low preferential separation of gas mixtures. The little or no selective transport could be due to the formation of pinholes either during membrane preparation or processing steps. This, in turn, would mainly be associated to the hard nature of PVA, which didn't soften the oxide phase sufficiently in the composite nanomembrane.

To overcome the low selective separation (which might reflect unsatisfactory mechanical stability) of the PVA/TiO_2 LBL nanomembrane, two measures were investigated (**Chapter 3**); (i) choosing a softer polymer with CO_2 selective properties, and (ii) changing the membrane architecture. Although no significant mechanical property enhancement was observed, compared to the PVA/TiO_2, the prepared PEG-OH/SiO_2 hybrid nanomembrane (Figure 1-5) demonstrated improved CO_2/N_2 selectivity.

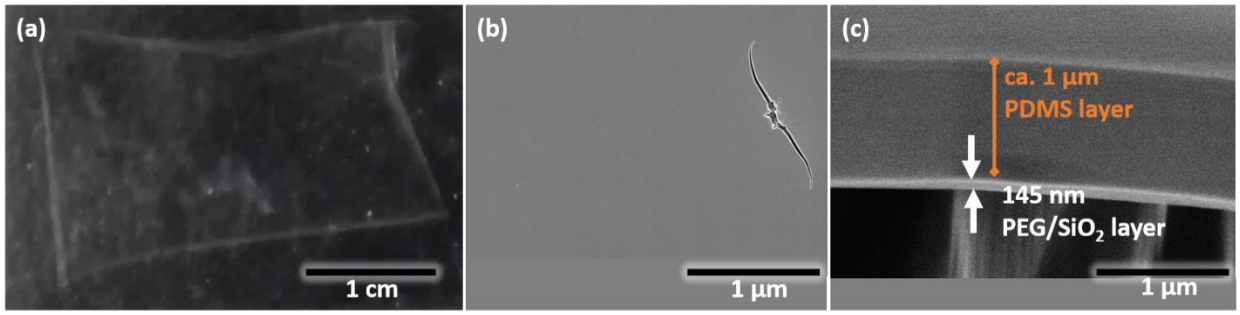

Figure 1-5. (a) Digital image of the nanomembrane in the detachment solvent. (b,c) SEM image of bare PEG/SiO_2 nanomembrane transferred onto a porous support; (c) after caulking layer coating to prevent leakage during gas separation experiment. Scale bar

The obtained results in Chapter 2 and Chapter 3 implied that it is not smooth to improve mechanical property of a nanomembrane while maintaining the separation performance or vice versa only by changing membrane materials. In fact, there can be a probability to tune both mechanical property and function together. It would, however, be time consuming and costly to search for the best material combinations. Therefore, a more reliable membrane architecture and preparation method was sought.

Accordingly, an unconventional design approach that integrates macroscopic mechanical stability together with tunable membrane functions was developed and presented in **Chapter 4**. This unique strategy involves the incorporation of aluminosilicate nanotube (ASNT) network structure (Figure 1-6a) as a bed scaffold to deposit polymeric membranes. Unlike amorphous metal oxides, aluminosilicate nanotubular oxide scaffolds brought about a dramatic enhancement in the mechanical property of the composite nanomembrane with polydimethylsiloxane (PDMS). A four-fold increase in the tensile strength and over 43 times higher biaxial modulus was observed compared to the pristine PDMS (Figure 1-6e,f).

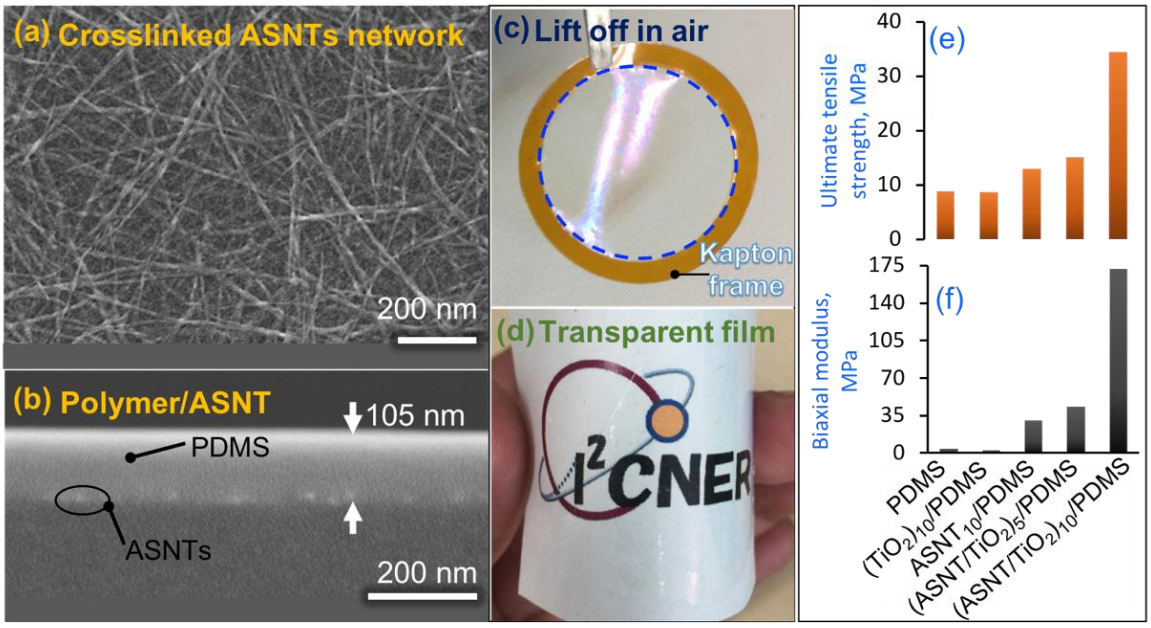

Figure 1-6. $(ASNT/TiO_2)_n$/PDMS nanomembrane. (a–d) Morphology and macroscopic manipulation. (e,f) Comparison of mechanical properties of pristine and scaffolded PDMS, confirming that ASNT networks brought about significant mechanical property enhancements.

Finally, summary and future prospect of the achievements of the study are provided in **Chapter 5**. The results section of each chapter is followed by a conceptual discussion. The dissertation presented a significant step-forward to the realization of ultrathin and free-standing, yet macroscopically tough advanced membranes for practical applications such as small molecule separation.

References

(1) Schummer, J. *Nat. Nanotechnol.* **2016**, *11* (10), 828–834.

(2) Maynard, A. D.; Aitken, R. J.; Butz, T.; Colvin, V.; Donaldson, K.; Oberdörster, G.; Philbert, M. A.; Ryan, J.; Seaton, A.; Stone, V.; Tinkle, S. S.; Tran, L.; Walker, N. J.; Warheit D. B. *Nature* **2006**, *444* (7117), 267–269.

(3) Wang, L.; Boutilier, M. S. H.; Kidambi, P. R.; Jang, D.; Hadjiconstantinou, N. G.; Karnik, R. *Nat. Nanotechnol.* **2017**, *12* (6), 509–522.

(4) Lindemann, P.; Tsotsalas, M.; Shishatskiy, S.; Abetz, V.; Krolla-Sidenstein, P.; Azucena, C.; Monnereau, L.; Beyer, A.; Gölzhäuser, A.; Mugnaini, V. *Chem. Mater.* **2014**, *26* (24), 7189–7193.

(5) Gupta, Y.; Hellgardt, K.; Wakeman, R. J. *J. Memb. Sci.* **2006**, *282* (1–2), 60–70.

(6) Schuster, C.; Rodler, A.; Tscheliessnig, R.; Jungbauer, A. *Sci. Rep.* **2018**, *8* (1), 1–11.

(7) Rogers, J. A.; Lagally, M. G.; Nuzzo, R. G. *Nature* **2011**, *477* (7362), 45–53.

(8) Liu, X.; Si, W.; Zhang, J.; Sun, X.; Deng, J.; Baunack, S.; Oswald, S.; Liu, L.; Yan, C.; Schmidt, O. G. *Sci. Rep.* **2015**, *4* (1), 7452.

(9) Li, Z.; Ma, G.; Ge, R.; Qin, F.; Dong, X.; Meng, W.; Liu, T.; Tong, J.; Jiang, F.; Zhou, Y. *Angew. Chem. Int. Ed.* **2016**, *55* (3), 979–982.

(10) Liu, Q.; Fujigaya, T.; Cheng, H.-M.; Nakashima, N. *J. Am. Chem. Soc.* **2010**, *132* (46), 16581–16586.

(11) Jiang, C.; Markutsya, S.; Pikus, Y.; Tsukruk, V. V. *Nat. Mater.* **2004**, *3* (10), 721–728.

(12) Fujie, T. *Polym. J.* **2016**, *48* (7), 773–780.

(13) Lu, X.; Yin, Y.; Zhang, L.; Xi, L.; Oswald, S.; Deng, J.; Schmidt, O. G. *Nano Energy* **2016**, *30*, 69–76.

(14) Fujie, T.; Ahadian, S.; Liu, H.; Chang, H.; Ostrovidov, S.; Wu, H.; Bae, H.; Nakajima, K.; Kaji, H.; Khademhosseini, A. *Nano Lett.* **2013**, *13* (7), 3185–3192.

(15) Watanabe, H.; Vendamme, R.; Kunitake, T. *Bull. Chem. Soc. Jpn.* **2007**, *80* (3), 433–440.

(16) Cheng, W.; Campolongo, M. J.; Tan, S. J.; Luo, D. *Nano Today* **2009**, *4* (6), 482–493.

(17) Huang, G.; Mei, Y. *Adv. Mater.* **2012**, *24* (19), 2517–2546.

(18) Mersha, A.; Selyanchyn, R.; Fujikawa, S. *CleanE* **2017**, *1* (1), 80–89.

(19) Kim, D.; Rogers, J. A. *ACS Nano* **2009**, *3* (3), 498-501.

(20) Ko, H. C.; Stoykovich, M. P.; Song, J.; Malyarchuk, V.; Choi, W. M.; Yu, C. J.; Geddes,

J. B.; Xiao, J.; Wang, S.; Huang, Y. *Nature* **2008**, *454* (7205), 748–753.

(21) Vandezande, P.; Gevers, L. E. M.; Vankelecom, I. F. J.; Koros, W. J.; Ma, Y. H.; Shimidzu, T.; Loeb, S.; White, L. S.; Wildemuth, C. R.; Stafie, N. *Chem. Soc. Rev.* **2008**, 37 (2), 365-405.

(22) Richardson, J. J.; Bjornmalm, M.; Caruso, F. *Science* **2015**, *348* (6233), 2491.

(23) Miyano, K.; Mori, A. *Thin Solid Films* **1989**, *168* (1), 141–149.

(24) Cho, J.; Char, K.; Hong, J. D.; Lee, K.-B. *Adv. Mater.* **2001**, *13* (14), 1076–1078.

(25) Koros, W. J. *Macromol. Symp.* **2002**, 188(1), 13-22.

(26) Vendamme, R.; Onoue, S.Y.; Nakao, A.; Kunitake, T. *Nat. Mater.* **2006**, *5* (6), 494–501.

(27) Dong, G.; Li, H.; Chen, V. *J. Mater. Chem. A* **2013**, *1* (15), 4610.

(28) Markutsya, S.; Jiang, C.; Pikus, Y.; Tsukruk, V. V. *Adv. Funct. Mater.* **2005**, *15* (5), 771–780.

(29) Zhu, X.; Tian, C.; Do-Thanh, C. L.; Dai, S. *ChemSusChem* **2017**, *10* (17), 3304–3316.

(30) Rajan, G. S.; Sur, G. I. L. S.; Mark, J. E.; Schaefer, D. W.; Beaucage, G. *J. Polym. Sci. Part B Polym. Phys.* **2003**, *41*, 1897–1901.

(31) Hosseini, S. S.; Li, Y.; Chung, T. S.; Liu, Y. *J. Memb. Sci.* **2007**, *302* , 207–217.

(32) Mahajan, R.; Burns, R.; Schaeffer, M.; Koros, W. J. *J. Appl. Polym. Sci.* **2002**, *86* (4), 881–890.

(33) Roy, N.; Sengupta, R.; Bhowmick, A. K. *Prog. Polym. Sci.* **2012**, *37* (6), 781–819.

(34) Bhattacharya, M. *Materials* **2016**, *9* (4), 1–35.

(35) Loos M. Fundamentals of polymer matrix composites containing CNTs. In *Carbon Nanotube Reinforced Composites*; Elsevier: Amsterdam, The Netherlands, **2015**; pp. 125–170.

(36) Liu, T.; Fan, W.; Zhang, C. *Polym. Nanotub. Nanocomposites Synth. Prop. Appl. Second Ed.* **2014**, 239–277.

(37) Kim, W. gwi; Nair, S. *Chem. Eng. Sci.* **2013**, *104*, 908–924.

(38) Kang, D. Y.; Lydon, M. E.; Yucelen, G. I.; Jones, C. W.; Nair, S. *ChemNanoMat.* **2015**, 1 (2), 102-108.

(39) Mersha, A.; Fujikawa, S. *ACS Appl. Polym. Mater.* **2019**, *1* (2), 112–117.

(40) Loos M. Composites. In *Carbon Nanotube Reinforced Composites*; Elsevier: Amsterdam, The Netherlands, **2015**; pp. 37–72.

(41) Vendamme, R.; Onoue, S.-Y.; Nakao, A.; Kunitake, T. *Nat. Mater.* **2006**, *5* (6), 494–501.

(42) Watanabe, H.; Kunitake, T. *Adv. Mater.* **2007**, *19* (7), 909–912.

Chapter 2 Preparation of large, ultra-flexible and free-standing nanomembranes of metal oxide/polymer composite and their gas permeation properties

Abstract

In this chapter, fabrication of free-standing nanomembrane of metal oxide (MO_x) and polymer by spin-assisted layer-by-layer (LBL) assembly is discussed. Although there are research works on the fabrication of free-standing nanomembranes, development of such membranes with sufficient macroscopic properties (to withstand mechanical stress) for applications such as separation remained a challenging task. By combining the flexibility of organic polymers and the rigidity of molecular networks in inorganic materials, a few tens nm thick, large size, highly flexible and free-standing composite nanomembrane was developed. Synergetic mechanical reinforcement was realized via sol-gel induced molecular level LBL assembly of MO_x and polymer. The nanomembrane sustained mechanical stability even after transfer onto a porous support for separation experiment. The electron microscopy observation proved no crack formation during nanomembrane fabrication and manipulation steps.

2.1 Introduction

Organic polymeric materials have been widely investigated in the fabrication of membranes, including scale up to industrial level, to take advantages of their flexibility and solution processability.[1] From application viewpoint, thin membranes provide several advantages such as low molecular transport resistance, thereby increase separation efficiency. But thinning polymeric membranes is often encountered by mechanical weakening which leads to defect formation as well as handling difficulty. Inorganic materials, on the other hand, are hard and brittle. They become highly fragile when processed into nanofilms.[1,2] Thus, combining organic and inorganic materials allows to integrate the flexibility of organic polymers and the rigidity of inorganic networks. The general properties of organic and inorganic materials with respect to membrane formation tendency are summarized in Figure 2-1. In addition to synergetic mechanical enhancement, organic/inorganic composite materials also offer distinct properties different from simple sums of original polymers and inorganics.[3]

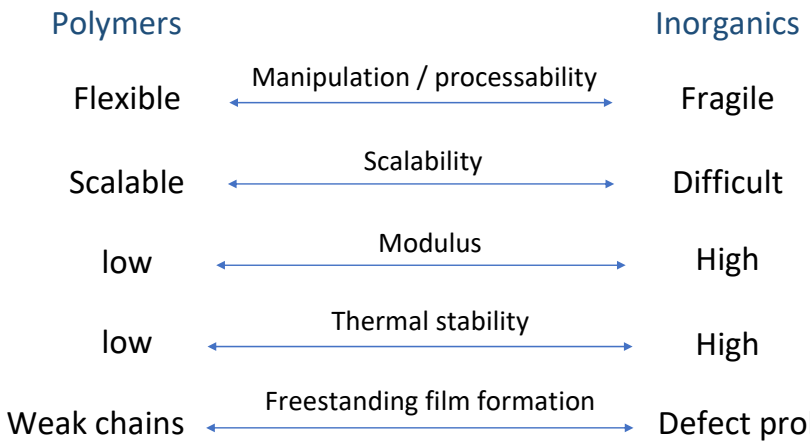

Figure 2-1. General comparison of organic and inorganic materials in regard to their tendency to form membranes.

Mechanically reinforced composite membranes are often prepared in either of two ways; (i) introduction of inorganic filler particles in to a polymer matrix or (ii) molecular level integration of organic and inorganic components. Incorporation of inorganic fillers such as metal oxides, and nanofibers into a polymer matrix[4–6] is a conventional method for improving mechanical property of polymeric membranes. In this approach, inorganic nanoparticles are introduced into the polymer solution prior to membrane formation. However, due to the likelihood of interfacial void formation,

such as plastic deformation[4], this method requires careful control of polymer−filler compatibility for suitable interfacial interactions and consequent membrane stability. Thus, it is still a crucial research task for the realization of defect-free membranes.[4,7,8]

In the second approach, molecular level designs such as organic/inorganic interpenetrating networks[3] and layer-by-layer (LBL) assembly[9] opened up opportunities for molecular level aggregation of membrane materials. Unlike to filler approach, such architectures allow higher proportion of organic/inorganic interaction sites, leading to a well-fused composite structure that enables the preparation of ultrathin and yet mechanically enhanced membranes. In addition to mechanical property improvement, incorporation of rigid inorganic structures into the polymer matrix creates molecular transport pathways[4], improving molecular flux. Furthermore, compositing organic and inorganic materials advances thermal stability,[10] allowing the deployment of such membranes at elevated temperature conditions.

Metal oxide (MO_x) and polymer composites are among the most promissing combinations to develop mechanically enhanced free-standing nanomembranes (FS-NMs). Spin-assisted LBL assembly, which was introduced by Kookheon Char's group,[11] is a suitable technique to adsorb metal oxide and polymer materials through chemisorption. The MO_x precursor and polymer phases undergo sol-gel reaction at the interface of alternate ultrathin coatings, leading to well-fused composite structure. The spin-assisted assembly yields a highly ordered internal structure via rearrangement of molecular chains and desorption of weakly bound chains. This simple technique allows multitude of membrane material selection, in part because it creates a platform to combine materials even from incompatible solvent solutions. Precise film thickness and surface roughness can also be controlled in molecular scale precision.

The general chemical reaction during sol–gel process can be described by the following three equations.[12]

$-M-OR + H_2O$	$\rightarrow$	$-M-OH + ROH$	Hydrolysis	(i)
$-M-OH + M-OR$	$\rightarrow$	$-M-O-M- + ROH$	Condensation	(ii)
$-M-OH + -M-OH$	$\rightarrow$	$-M-O-M- + H_2O$	Condensation	(iii)

In this chapter, the preparation of an ultrathin, large size composite nanomembrane by spin-assisted alternate chemisorption of molecular layers of TiO_2 and poly(vinyl alcohol) (PVA) has been discussed. Although LBL assembled polymer/inorganic composite films have been

investigated before,[3,13] this work presents essential features, including free-standing nature coupled with pin-hole freeness as confirmed by gas permeation test. To the best of my knowledge, experimental demonstration of gas permeation using such free-standing MO_x/polymer composite nanomembranes have not been studied.

2.2 Experimental Section

2.2.1 Materials

Soda lime glass was used as substrate for membrane preparation. Poly(4-vinylphenol) (PVP, M_w=11000, Sigma-Aldrich) was used as sacrificial layer. Poly (vinyl alcohol) (M_w=78000, 88 mol % hydrolyzed, Polysciences, Inc.) was used as polymer layer precursor. Titanium *n*-butoxide ($Ti(O^nBu)_4$, Gelest Inc.) was used as metal oxide precursor. Ethanol (EtOH, anhydrous, EMSURE, Germany) and toluene (Wako Co., Ltd.) were used as received. Deionized water (18.3 MΩ cm^{-1}, Millipore, Direct-QTM) was used for rinsing and solution preparation.

2.2.2 Nanomembrane preparation

The FS-NMs preparation process is illustrated schematically in Figure 2-2. It involves three steps; (i) sacrificial layer coating, (ii) LBL membrane assembly and (iii) membrane detachment by selective dissolution of the sacrificial layer.

Firstly, a glass substrate was sonicated in EtOH for about 60 min, rinsed by deionized water, dried by air-blowing and treated with oxygen plasma (FA-1, SAMCO, Japan, RF power: 55 W, the flow rate of oxygen: 10 sccm, chamber pressure: 20 Pa) for 4 min to make the substrate surface hydrophilic. Water contact angle after O_2 plasma etching is < 10º. Afterwards, a 15 wt% EtOH solution of PVP was spin-coated (3000 rpm, 60 sec) on the glass substrate and heated at 120 °C for 5 min.

Once cooled down to room temperature, an aqueous solution of PVA (0.3 wt %) was deposited (3000 rpm, 2 min) on the sacrificial layer, and allowed to dry in ambient air for 1 hour. The PVA coating introduces hydroxyl groups that are essential for the formation of well-integrated sreucture with metal oxide.[14] Then, a $Ti(O^nBu)_4$ solution (50 mM, in toluene) was spin coated (3000 rpm, 2 min) and left in an ambient air for 30 min to allow hydrolysis and condensation. This alternate sol-gel deposition cycle of PVA and TiO_2 was repeated until the desired film thickness.

PVA/TiO_2 film growth during the repetitive process was monitored by parallelly preparing the LBL film on a quartz plate, and measuring UV/Vis absorption (Jasco V-670) after each deposition cycle.

Lastly, the glass substrate was immersed in EtOH to dissolve the sacrificial PVP layer and release the self-supporting nanomembrane. The detached film was freely floating in the sub-surface of EtOH solution.

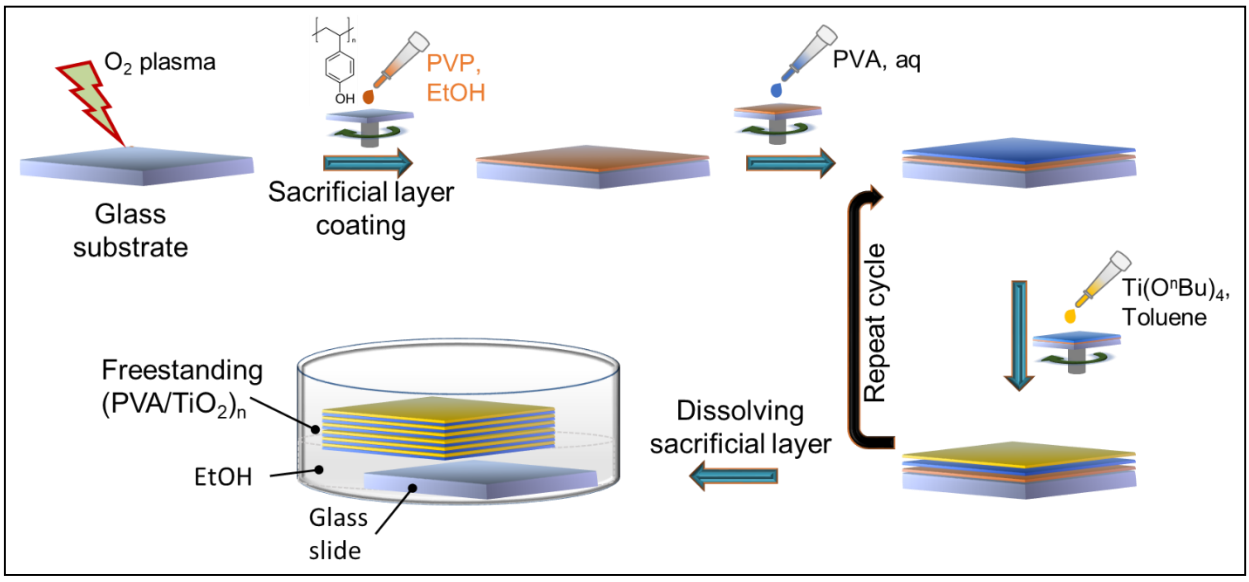

Figure 2-2. Schematic representation of nanomembrane fabrication process by spin-assisted LBL assembly.

Film thickness and surface morphology were observed by field emission scanning electron microscope (FE-SEM, Hitachi S-5200). Specimen for SEM observation was prepared by transferring the nanomembrane onto anodized porous alumina (Anodisc, G.E. Healthcare) support.

2.2.3 Gas permeation experiment

In order to evaluate gas permeation, nanomembranes were transferred onto a porous alumina support. In fact, any porous support can be employed as long as its surface is smooth in order to prevent the nanomembrane from damage. After that, membrane area (space through which gas molecules pass) was limited by Kapton and alumina tapes with the open hole of 1 cm diameter as shown in Figure 2-3a. Subsequently, it was placed in the membrane cell (Figure 2-3b) to test gas permeation.

Gas permeation was measured using a commercial instrument (GTR-11A/31A system, GTR Tec Corp., Japan) coupled to gas chromatography, and the overall experimental setup is described schematically in Figure 2-3b. A mixed gas was introduced to the feed side of the membrane cell at room temperature. The pressure of the feed gas was set at 100 kPa as a gauge pressure, whilst

the permeate side was maintained in vacuum condition, resulting in a total pressure difference of ca. 200 kPa. The volume of gas passed through the membrane per unit time was measured by gas chromatography.

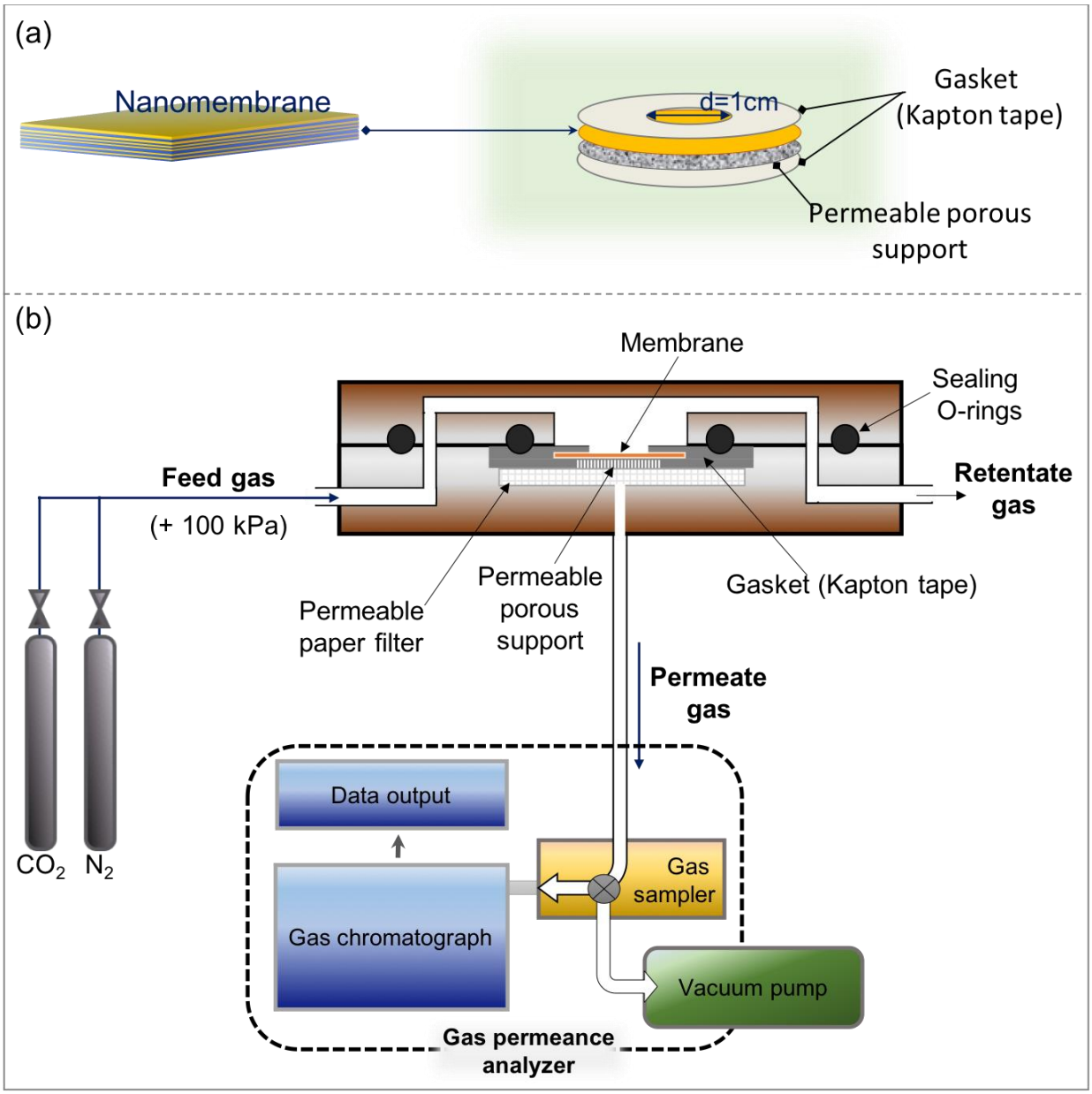

Figure 2-3. A schematic illustration of (a) nanomembrane assembly for gas permeation experiment, (b) gas permeance measurement apparatus.

From the obtained volume, gas permeance (*P*) and separation factor (α) were calculated according to the following equations;

$$P = \frac{N}{A \,.\, \Delta P} \qquad \text{(Eq. 2-1)}$$

$$\alpha = \frac{P_{CO2}}{P_{N2}} \qquad \text{(Eq. 2-2)}$$

where N (m^3/sec) refers to the flow rate measured on the permeate side, A (m^2) is effective membrane area and ΔP (Pa) is pressure difference between the feed and permeate side. In all the experiments, the effective area of gas permeation was 0.785 cm^2. For easier comparison permeance was reflected in the common GPU unit, where 1GPU = 7.5×10^{-12} $m^3/m^2{\cdot}s{\cdot}Pa$, at standard temperature and pressure conditions.

2.3 Results and discussion

2.3.1 Definition of important terms

To avoid confusion with terminology, the following definitions are provided.

- Membrane:

  The prepared film that does not include the porous support.

- Free-standing nanomembrane (FS-NM):

  A nanometer-thick membrane with self-supporting property, which is able to physically separate two spaces by sustaining its size and shape without support.[15,16] It does not include porous support.

- Porous support:

  A highly gas permeable physical support onto which FS-NM is placed for gas permeance experiment.

- Double layer nanomembrane:

  A membrane which consisted of MO_x layer coated on to a polymer layer.

- Layer-by-layer nanomembrane:

  A membrane comprising multiple LbL coating of MO_x and polymer.

2.3.2 Membrane design

Double layer nanomembranes of MO_x and polymers such as ZrO_2/(PEI-PCGF)[16] suffer from defects. This is because the polymer and MO_x layers exist distinctly in the membrane, which results in obvious ceramic nature of the MO_x layer. Meaning that the polymer has little opportunity to penetrate into the MO_x network, and vice versa. Mechanical reinforcement is, therefore, minimal. To overcome this fragility problem, a sequential spin-coating of thin layers of polymer and TiO_2 was proposed to allow molecular level fusion of the components. Accordingly, PVA was employed as a polymer component since it has rich hydroxyl groups on its continuous chain. The -OH groups react readily with metal alkoxides through sol-gel process.

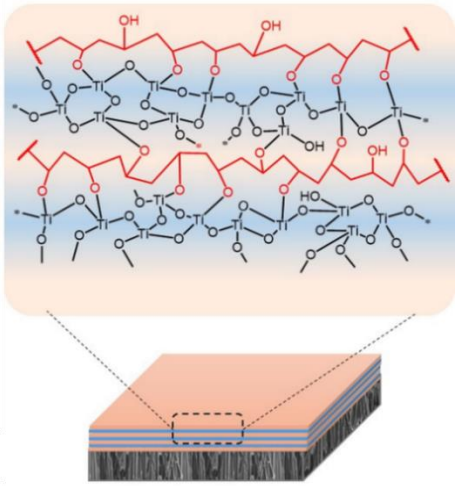

Figure 2-4. Schematic representation of the internal structure of LbL assembled $(PVA/TiO_2)_n$ nanomembrane.

2.3.3 Film growth monitoring, morphological and mechanical properties

The nature of film growth was evaluated by measuring UV/Vis absorbance after each TiO_2 coating. Test sample was prepared directly on quartz glass along with the FS-NMs. UV/Vis spectra of 5 cycles of PVA/TiO_2 deposition is shown in Figure 2-5a. The linear increase in absorbance of TiO_2 at 252 nm against the cycles of deposition (Figure 2-5b) implied that TiO_2 layer of similar thickness was deposited at each cycle. The UV-Vis observation is unable to track the deposition of PVA. However, earlier works suggested that PVA is readily anchored to the titanium alkoxide due to abundancy of hydroxyl groups on its surface.[14]

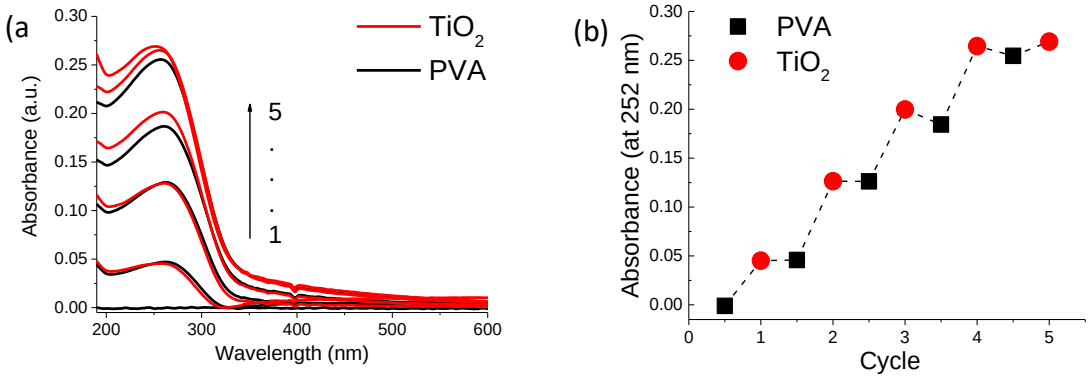

Figure 2-5. (a) UV/Vis absorption spectra of sequential PVA/TiO_2 deposition, (b) UV/Vis absorbance at 252 nm of consecutive PVA and TiO_2 layers.

Large-size self-supporting nanomembrane was obtained after dissolving the sacrificial layer in EtOH (Figure 2-6a). This step is also illustrated schematically in Figure 2-2. The nanomembrane suspended freely in the detaching solvent. The scanning electron microscope investigation showed that the fabricated nanomembrane has smooth and uniform surface (Figure 2-6b). Large defects or cracks were not seen under SEM, even after macroscopic manipulations. Figure 2-6d demonstrates the cross-sectional views of a 60 nm thick PVA/TiO_2 FS-NM after being transferred onto a porous alumina support. The membrane consisted of 6.5 cycles (13 alternate layers of PVA and TiO_2). The membrane thickness was uniform throughout, and the average thickness for one cycle deposition of PVA and TiO_2 is estimated to be about 10 nm. From this, the thickness of a single layer of PVA or TiO_2 can roughly be estimated as ~ 5 nm. In fact, the hydrodynamic radius of PVA with 78900 g/mol (which is close to that of PVA used in the present experiment) in solution is about 15 nm.[17] The corresponding radius of PVA chains in the solid film should be smaller than 15 nm. Thus, the PVA monolayer may not rough the surface of each PVA/TiO_2 bilayer, resulting in smooth PVA/TiO_2 multilayer membrane.

Although layered morphologies were vaguely seen in the membrane's cross-sectional image (Figure 2-6c), no inter-space between layers was observed, suggesting that the layers were well adhered. The good interfacial fusion could be facilitated by the sol-gel reaction at the PVA-TiO_2 interface. The ultrathin coating of membrane components (~ 5 nm) also plays an important role for the formation of well-integrated membrane structure.

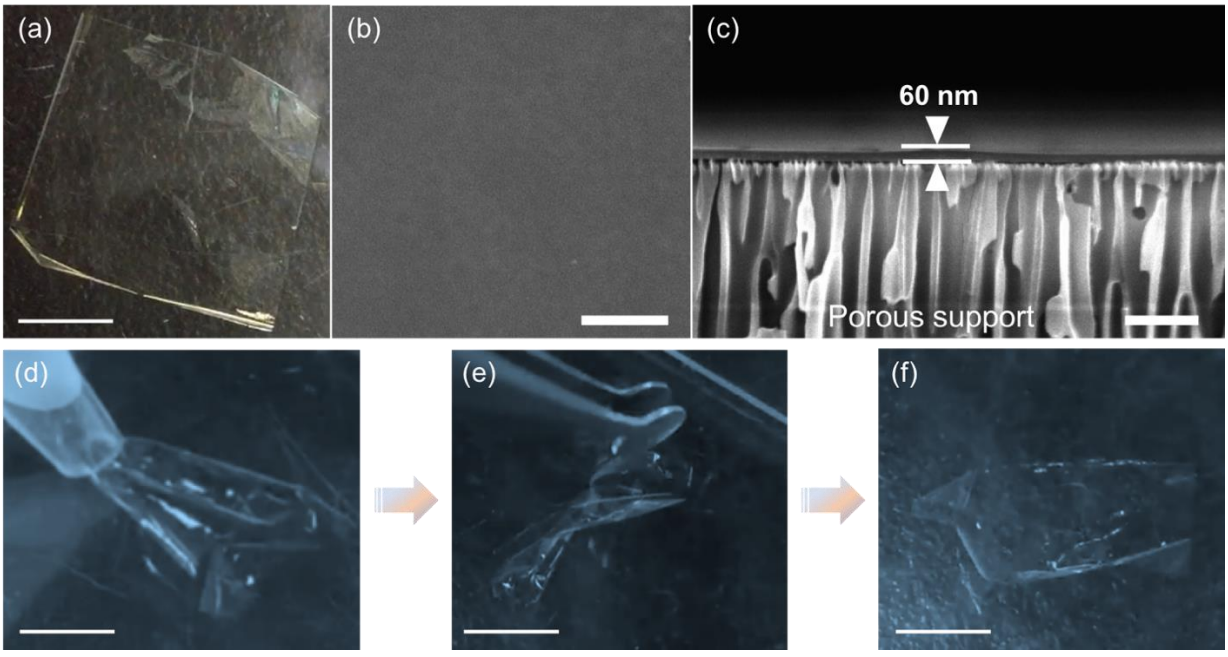

Figure 2-6. LbL assembled $(PVA/TiO_2)_{6.5}$ composite nanomembranes. (a) Digital photograph of the detached large-size FS-NM (ca. 10 cm^2) floating on EtOH solution. (b) Surface and (c) cross-sectional view SEM images of the FS-NMs transferred onto a porous alumina (Anodisc) support. (d–f) Digital photographs showing the aspiration and release process of a centimeter-scale nanomembrane into a micropipette: (d) aspiration (e) assistance by a tweezer to stretch the folding (f) stretched nanomembrane. **Scale bars**: Digital images **1 cm**, SEM images **500 nm**.

The prepared nanomembrane was very flexible as demonstrated by the aspiration and release process of a centimeter-scale nanomembrane through a micropipette with a hole diameter of 2 mm (Figure 2-6d). The detached membrane, which was floating in EtOH, was aspirated into the micropipette and released back to the solvent. The membrane undergoes multiple bending to fit the mouth of the micropipette during the sacking/release process. Once released into the solvent, the film regained its original shape and size through a simple assistance by a laboratory tweezer (Figure 2-6e, f). The excellent flexibility could be explained by the molecular level fusion of the membrane components. The ultrathin PVA network surrounds the ultrathin amorphous rigid structure of TiO_2 forming a multiple sandwich type structures, this in turn allows the movement TiO_2 layer to bend along with PVA without breaking.

A PVA/TiO_2 nanomembrane consisted of as low as 3 cycles (ca. 30 nm thick) could be detached, and successfully transferred onto a porous support without any significant damage. However, membranes under 50 nm thickness didn't show reproducible gas permeation resistance. This should be attributed to the presence of pin-holes possibly formed during membrane manipulation (such as detachment, transferring onto porous support or during set up for permeance experiment).

2.3.4 Gas permeation property

Gas permeation of the $(PVA/TiO_2)_{6.5}$ nanomembrane was tested for two purposes; in order to evaluate the degree of defects in the membrane as well as to study the gas separation behavior of the membrane materials.

A N_2/CO_2 (95:5) mixture gas was used, and the permeance and CO_2/N_2 selectivity of ca. 60 nm thick nanomembrane was determined based on Equations 2-1 and 2-2. The results are presented in Figure 2-7. The membrane showed low gas permeance property, in part, demonstrating that the nanomembrane did not have serious defects or pin-holes that can lead to gas leakage. This is essential from FS-NM design perspective. However, the low permeance is not desirable from

separation viewpoint. The weak affinity of PVA and TiO_2 towards CO_2 could be a possible reason for the low permeance and CO_2/N_2 selectivity. But it is difficult at this point to illuminate the contribution of cracks for low separation performance of the PVA/TiO_2 nanomembrane.

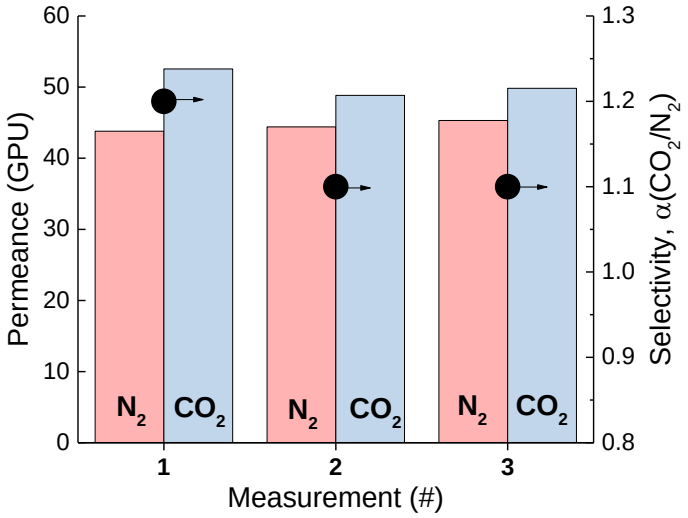

Figure 2-7. Gas permeance property of the PVA/TiO_2 multilayer nanomembrane.

2.4 Discussion

Figure 2-4 shows the schematic illustration of the prepared PVA/TiO_2 multilayer nanomembrane. Although the gas permeation property of the nanomembrane was not satisfactory (being several orders smaller compared to conventional gas separation polymer membranes), the membrane structure suggests useful features in nanomembrane development.

In simple metal oxide/polymer double layer nanomembranes,[16] it was difficult to achieve structural integrity of the polymer and MO_x layers that leads to breaking of the MO_x layer. On the other hand, LBL assembly proves the way for molecular fusion of ultrathin layers of MO_x and polymer. Such multiple molecular scale fusion introduces macroscopic flexibility and robustness to the composite nanomembrane. This could be because the continuous polymer networks in the alternate coatings protect the MO_x layers from breaking.

2.5 Conclusion

Large size, ultrathin (~ 50 nm) and freestanding organic/inorganic composite nanomembrane was prepared by spin-assisted LbL assembly of TiO_2 and PVA. The nanomembrane did not have serious defects, even after transfer onto a porous support, as confirmed by SEM observation and gas permeation test. It also demonstrated excellent flexibility during macroscopic manipulation without any film fragmentation.

References

(1) Koros, W. J. *Macromol. Symp.* **2002**, 188 (1), 13-22.

(2) Byrd, H.; Holloway, C. E.; Pogue, J.; Kircus, S.; Advincula, R. C., Knoll, W. *Langmuir*, **2000**, *16* (26), 10322–10328.

(3) Vendamme, R.; Onoue, S.Y.; Nakao, A.; Kunitake, T. *Nat. Mater.* **2006**, *5* (6), 494–501.

(4) Dong, G.; Li, H.; Chen, V. *J. Mater. Chem. A* **2013**, *1* (15), 4610.

(5) Zhu, X.; Tian, C.; Do-Thanh, C.-L.; Dai, S. *ChemSusChem* **2017**, *10* (17), 3304–3316.

(6) Rajan, G. S.; Sur, G. I. L. S.; Mark, J. E.; Schaefer, D. W.; Beaucage, G. *J. Polym. Sci. Part B Polym. Phys.* **2003**, *41*, 1897–1901.

(7) Kim, W. gwi; Nair, S. *Chem. Eng. Sci.* **2013**, *104*, 908–924.

(8) Galizia, M.; Chi, W. S.; Smith, Z. P.; Merkel, T. C.; Baker, R. W.; Freeman, B. D. *Macromolecules* **2017**, *50* (2), 7809-7843.

(9) Richardson, J. J.; Bjornmalm, M.; Caruso, F. *Science* **2015**, *348* (6233), 2491.

(10) Xu, Z. L.; Yu, L. Y.; Han, L. F. *Front. Chem. Eng. China* **2009**, *3* (3), 318–329.

(11) Cho, J.; Char, K.; Hong, J. D.; Lee, K. B. *Adv. Mater.* **2001**, *13* (14), 1076–1078.

(12) Schubert, U. Chemistry and Fundamentals of the Sol–Gel Process. In: Schubert, U.; Hüsing, N. editors. *Synthesis of Inorganic Materials*; 3rd edn, VCH-Wiley Verlag GmbH, Weinheim, Germany, 2012; pp. 1-28.

(13) Byrd, H.; Holloway, C. E.; Pogue, J.; Kircus, S.; Advincula, R. C.; Knoll, W. *Langmuir* **2000**, *16* (26), 10322-10328.

(14) Hashizume, M.; Kunitake, T. *Langmuir* **2003**, *19* (24), 10172–10178.

(15) Huang, G.; Mei, Y. *Adv. Mater.* **2012**, *24* (19), 2517–2546.

(16) Mersha, A.; Selyanchyn, R.; Fujikawa, S. *CleanE* **2017**, *1* (1), 80–89.

(17) Budhlall, B. M.; Landfester, K.; Sudol, E. D.; Dimonie, V. L.; Klein, A.; El-Aasser, M. S. *Macromolecules* **2003**, *36* (25), 9477–9484.

Chapter 3 Metal oxide/polymer blends for the preparation of free-standing nanomembranes and their gas permeation properties

Abstract

In this chapter, the development of free-standing nanomembrane (FS-NMs) from a blended type of organic/inorganic composites has been discussed. Blending approach can offer atomic scale *in-situ* interaction of organic and inorganic structures in a membrane. Here, a hydroxyl-terminated polyethylene glycol (PEG-OH) and silicon tetraisocyanate were premixed, and spin-coated to prepare FS-NMs. PEG-OH has been selected as a polymer precursor to take advantage of its compatibility with metal oxides for sol-gel reaction and its CO_2 solubility-selectivity behavior. Although no mechanical property enhancement was observed, compared to the PVA/TiO_2 LBL nanomembrane discussed in Chapter 2, the PEG/SiO_2 hybrid membrane demonstrated improved CO_2/N_2 selectivity.

3.1 Introduction

Polymeric films become weak upon thinning to a nanometer-scale and some polymers are difficult to spun into ultrathin films,[1] making it unfavorable to prepare purely organic free-standing nanomembranes (FS-NMs). On the other hand, inorganic materials are rigid and difficult to handle as nanomembranes. Organic/inorganic composite materials combine these conflicting features of polymers and inorganics, and thus, enable the development of mechanically enhanced self-supporting nanomembranes.[2]

In addition to incorporation of inorganic fillers into a polymer matrix, composite membranes are prepared by molecular scale integrations such as layer by layer (LBL) assembly[2,3] and simply blending the organic and inorganic components prior to membrane preparation.[4] This molecular scale approaches enable atomic or molecular level interactions that are essential for the development of mechanically reinforced FS-NMs. Apart from mechanical reinforcement, composite membranes possess higher thermal stability,[5] compared to the pristine polymer.

According to Kunitake's group,[4] organic/inorganic hybrid interpenetrating networks are interesting pathways to prepare FS-NMs of only a few tens nanometer thickness with large macroscopic size and flexibility. They fabricated nanomembranes from blend formula of the corresponding metal oxide and polymer precursors. But the membranes were not tested for applications such as separation. Similarly, tough hydrogel membranes with micrometer-scale thickness have been developed via non-covalent double network strategy by Gong's[6] and other groups[7] for potential applications such as post-operative antiadhesive and biosensor membranes.

These mechanically robust materials are the motivations to the present work for preparing ultrathin separation membrane employing organic/inorganic hybrid materials. In this work, a metal oxide/polymer hybrid FS-NM was prepared by blending the components prior to membrane fabrication (Figure 3-1). Blending approach can offer atomic scale *in-situ* interaction of organic and inorganic structures in a membrane. As discussed in Chapter 2, I previously prepared free-standing and ultrathin PVA/TiO_2 composite membrane via LBL assembly. Despite large lateral size and macroscopic flexibility of the nanomembranes, the CO_2/N_2 separation performance was not satisfactory. In addition to the weak CO_2 affinity of PVA, the low separation performance (especially low selectivity) could be associated to pinholes formed either during membrane

preparation or processing steps. This, in turn, may come from the hard nature of the nanomembrane where PVA didn't soften the oxide phase sufficiently.

Thus, in addition to changing the membrane architecture, a softer polymer with more CO_2 affinity property was employed aiming to prepare mechanically stable, yet CO_2 selective nanomembrane.

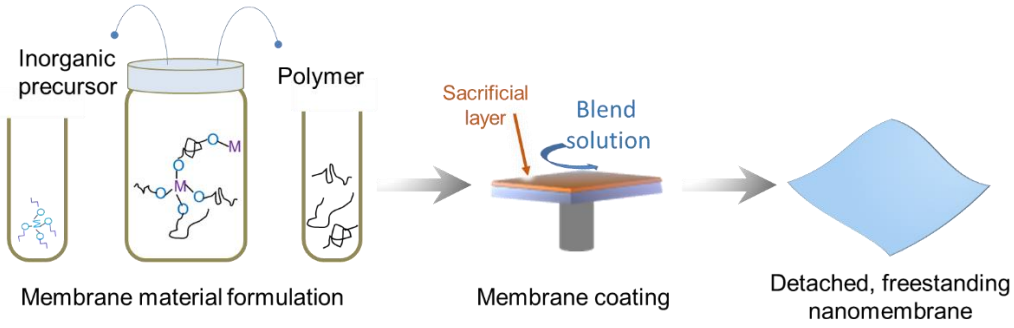

Figure 3-1: General representation of hybrid nanomembrane preparation process.

Hydroxyl-terminated polyethylene glycols (PEG-OH) are potential candidates due to their compatibility with metal oxides for sol-gel reactions (Figure 3-1), and their CO_2 solubility selectivity behavior.[8] Alkoxides are often used as metal oxide precursors. In this study, however, silicon tetraisocyanate was utilized as a source of SiO_2 due to its good reactivity, compared to alkoxides. Like alkoxides, the sol-gel reaction involving $Si(NCO)_4$ goes readily to completion as confirmed by previous study.[9]

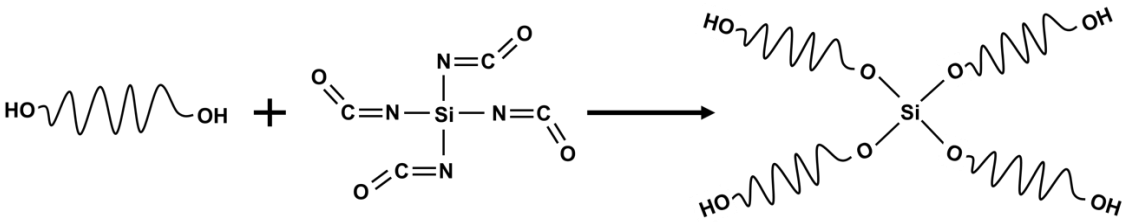

Figure 3-2: Scheme for the formulation of organic/inorganic blend material.

In this chapter, the preparation of PEG-OH/SiO_2 hybrid nanomembrane with preferential selectivity to CO_2 over N_2 has been presented. In order to completely avoid gas leakage, a caulking layer of polydimethylsiloxane (PDMS)[10] was employed. To the best of my knowledge, gas permeation properties of such hybrid and free-standing ultrathin membranes have not been studied.

3.2 Experimental Section

3.2.1 Materials

Silicon wafer with 350 µm thickness and glass substrate were used to spin-coat nanomembranes. Poly(4-vinylphenol) (PVP, M_w=11000, Sigma-Aldrich) was used as a sacrificial layer. Polyethylene glycol (M_w=2000, Wako Ltd.) was employed as a polymer precursor. Silicon tetraisocyanate $(SiNCO)_4$ (Matsumoto Fine Chemicals Co., Ltd.) and Titanium *n*-Butoxide ($Ti(O^nBu)_4$, Gelest Inc.) were used as metal oxide precursors. Polydimethylsiloxane (PDMS, Sylgard® 184) was used as caulking layer. Ethanol, chloroform and n-hexane were purchased from Wako Co., Ltd. and used as received. Deionized water (18.3 MΩ cm^{-1}, Millipore, Direct-QTM) was used for rinsing and solution preparation.

3.2.2 Nanomembrane preparation

In the preliminary step, separate solutions of $Si(NCO)_4$ and PEG-OH were prepared in chloroform, and slowly mixed to prepare blend solutions of PEG-OH and $Si(NCO)_4$ in varying ratios (Table 3-1). In the meantime, a glass substrate was cleaned by sonication in EtOH for 60 min and subsequent rinsing by deionized water. The glass substrate was dried by air-blowing and treated with oxygen plasma for 4 min to hydrophilize its surface (the oxygen plasma treatment is described in Chapter 2). Afterwards, a PVP (15 wt%, in EtOH) sacrificial layer was spin-coated (3000 rpm, 60 sec) on the glass substrate and heated at 120 °C for 5 min.

Table 3-1. PEG-OH and $Si(NCO)_4$ ratio optimization from the view point of reactive sites and membrane formation tendency.

S/N		1	2	3	4	5	6
Molar ratio (PEG-OH/SiO_2)		9:1	4:1	2:1	1:1	1:2	1:4
Concentration (Total = 400 mM)	PEG-OH	360	320	268	200	132	80
	SiO_2	40	80	132	200	268	320

Once cooled down to room temperature, a PEG-OH/SiO_2 blend solution was deposited on the pre-coated sacrificial layer at 3000 rpm for 2 min, and heated at 100 ºC for 12 hrs. For membranes to be used in gas permeation test, a 10 wt% PDMS caulking layer was spin-coated. Finally, the glass substrate was immersed in ethanol to dissolve the sacrificial layer and release the free-standing

nanomembrane. The overall membrane preparation process is illustrated schematically in Figure 3-3.

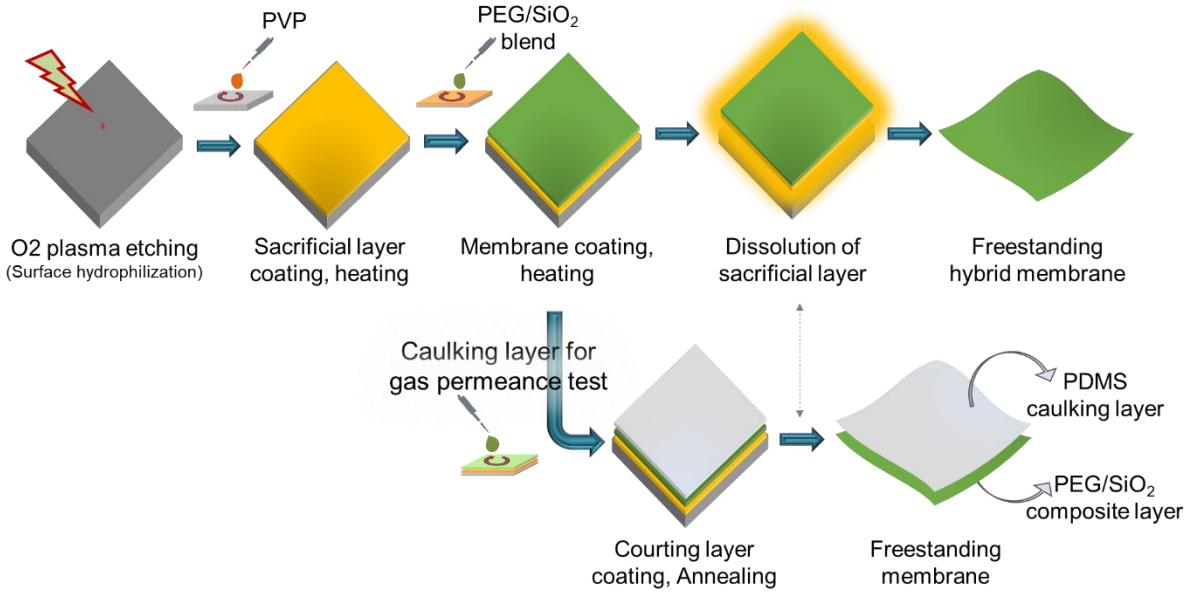

Figure 3-3. Schematic representation of nanomembrane fabrication process by spin-coating.

Film thickness and surface morphology were investigated by field emission scanning electron microscope (FE-SEM, Hitachi S-5200). Specimen for surface observation was prepared by transferring the nanomembrane onto supports such as anodized porous alumina (Anodisc, G.E. Healthcare).

3.2.3 Gas permeation experiment

For gas permeation test, the prepared nanomembranes were transferred onto a porous polyimide support. After transfer onto a porous support, membrane area (space through which gas molecules pass) was limited by Kapton tape with the open hole of 1 cm diameter as illustrated in Figure 2-3a, Chapter 2.

Subsequently, the membrane was placed in a home-made membrane cell, and gas permeation was measured using a bubble flow meter (Figure 3-4 below). The pure gas flow rate in cm^3/min of CO_2 and N_2 was measured and converted into permeance (P) using the following equation. Selectivity (α) was also determined as the ratio of permeance.

$$P = \frac{N}{A \cdot \Delta P} \qquad \text{(Eq. 3-1)}$$

$$\alpha = \frac{P_{CO2}}{P_{N2}} \qquad \text{(Eq. 3-2)}$$

where N (m^3/sec) refers to the flow rate measured on the permeate side, A (m^2) is effective membrane area and ΔP (Pa) is pressure difference between the feed and permeate side. In the experiment, effective area of gas permeation was 0.785 cm^2. For convenience, permeance was reflected in the common GPU unit, where 1GPU = 7.5×10^{-12} $m^3/m^2\cdot s\cdot Pa$, at standard temperature and pressure conditions.

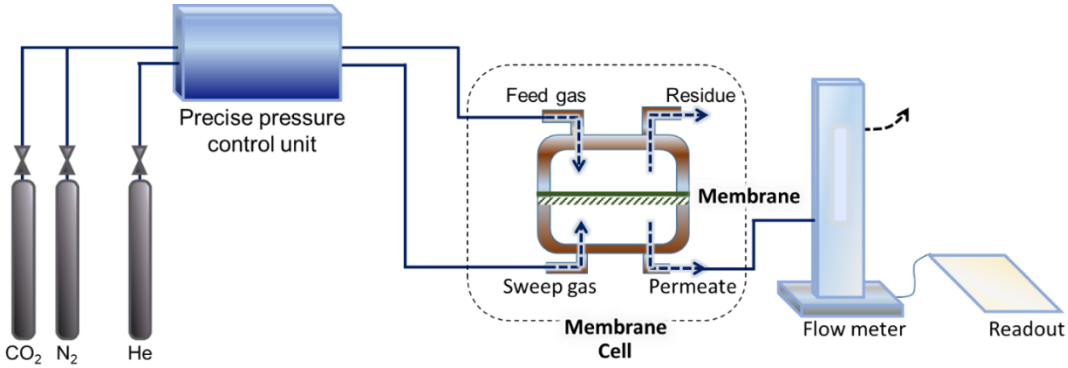

Figure 3-4. Single gas permeation measurement apparatus. The flow rate of CO_2 and N_2 was measured separately and transformed into permeance. Helium was used as a sweep gas in both cases. The feed gas volume and pressure conditions were set at 100 sccm and 0.2 MPa, respectively.

3.3 Results and discussion

3.3.1 Membrane material selection and preparation conditions

In preparing a blend solution, suitable mixing ratio of the polymer and MO_x precursor is very important for homogenous distribution of organic and inorganic structures. The PEG-OH/SiO_2 ratio was determined based on the sol-gel reactive sites of the PEG-OH and MO_x precursor; i.e., the number of OH-groups per mole of PEG-OH and the number of NCO-groups in $Si(NCO)_4$. PEG-OH has two reactive sites and $Si(NCO)_4$ has four reactive sites per mole. Thus, stoichiometrically, 2 moles of PEG-OH react with 1 mole of $Si(NCO)_4$ (i.e., PEG-OH/$Si(NCO)_4$ ratio of 2:1).

Based on this, wide range of ratios were prepared and evaluated for their film formation behavior. The result is summarized in Table 3-2. Also, the effect of temperature on membrane formation and stability was studied. Films were annealed at 100 ºC to facilitate the sol-gel reaction.

Table 3-2. PEG-$(OH)_2$/$Si(NCO)_4$ ratio optimization from the viewpoint of membrane formation behavior.

<table>
<tr><th rowspan="2">Annealing condition</th><th colspan="6">PEG-$(OH)_2$/$Si(NCO)_4$ ratio*</th></tr>
<tr><th>9:1</th><th>4:1</th><th>2:1</th><th>1:1</th><th>1:2</th><th>1:4</th></tr>
<tr><td>Ambient, 12hrs</td><td colspan="2">No film</td><td colspan="2">Film formed, but fragile</td><td colspan="2" rowspan="2">Solution was not stable for film preparation (Fast hydrolysis)</td></tr>
<tr><td>100 ºC, 12 hrs</td><td colspan="2">Non-detachable film</td><td colspan="2">Stable free-standing film</td></tr>
</table>

*Molar ratio; PEG-OH : $Si(NCO)_4$

As can be seen in Figure 3-5 and Table 3-2, there was an obvious enhancement in the chemical and mechanical stabilities of the prepared nanomembranes after thermal treatment, compared to ambient condition. This should be because heating facilitated the sol-gel crosslinking reaction. Accordingly, stable free-standing PEG-OH/SiO_2 hybrid nanomembranes were obtained from thermally annealed 2-to-1 and 1-to-1 combination of PEG-OH/$Si(NCO)_4$. The membranes maintained their shape and size after detachment from substrates.

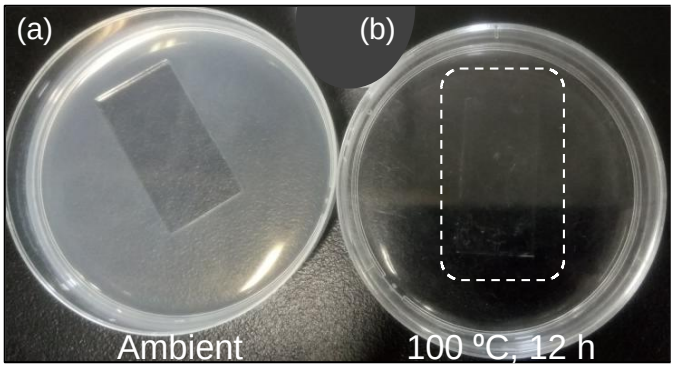

Figure 3-5. Digital images showing the difference in the stability of the PEG-OH/$Si(NCO)_4$ films during immersion in EtOH for detachment. (a) PEG-OH/$Si(NCO)_4$ film directly immersed in EtOH. The murky appearance of the solution indicates the dissolution of membrane components. (b) PEG-OH/$Si(NCO)_4$ film immersed in EtOH after annealing at 100 ºC. Solution remained clear implying that no new species was introduced into the solvent, except the PVP sacrificial layer.

3.3.2 Morphological and mechanical properties

In addition to blending ratio and annealing temperature, it is worth explaining that the reactivity of the MO_x precursor affects the membrane formation and subsequent mechanical properties. As discussed in Chapter 2, $Ti(O^nBu)_4$ was used as a MO_x precursor to prepare PVA/TiO_2 composite nanomembrane. However, when replacing PVA by polyethylene glycol (for its softer nature with CO_2 affinity property) to make PEG/TiO_2 nanomembranes, the membranes became more fragile, even under heating at 70 ºC for 12 hrs. The appearance of the nanomembranes is shown in Figure 3-6. Although the annealing temperature (70 ºC) was milder than the PEG-OH/SiO_2 case (100 ºC), the main reason for film fragility could be attributed to lesser sol-gel reactivity of PEG-OH relative to PVA. Apparently, this could be due to lesser proportion of -OH groups in PEG-OH than PVA. Therefore, $Si(NCO)_4$ was tested instead of $Ti(OnBu)_4$ as a MO_x precursor to compensate the milder reactivity of PEG-OH.

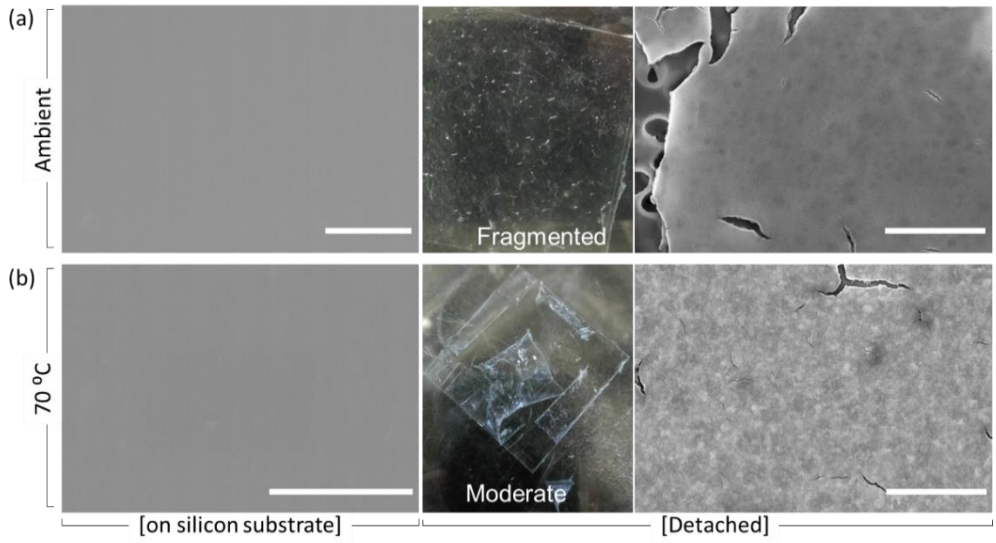

Figure 3-6. Nature of PEG-OH/TiO_2 hybrid nanofilm under ambient condition (a) and annealing at 70 ºC for 12 hrs (b). **Scale bar: 1 µm**.

Interestingly, a better integrity with PEG-OH has been observed, leading to the realization of large size (Figure 3-7a), stable nanomembrane that can be detached and transferred onto a porous support without significant damage. As mentioned above, thermally annealed 2-to-1 and 1-to-1 molar ratios of PEG-OH/$Si(NCO)_4$ form large size nanomembranes.

However, despite successful preparation of large size PEG-based nanomembrane, cracks were observed under SEM (Figure 3-7b,c). It was seen from physical manipulation and SEM observation that the PEG-OH/SiO_2 nanomembrane has rigid nature. Although the mechanical property of this membrane was not satisfactory, I considered evaluating its gas separation property as a proof of design concept.

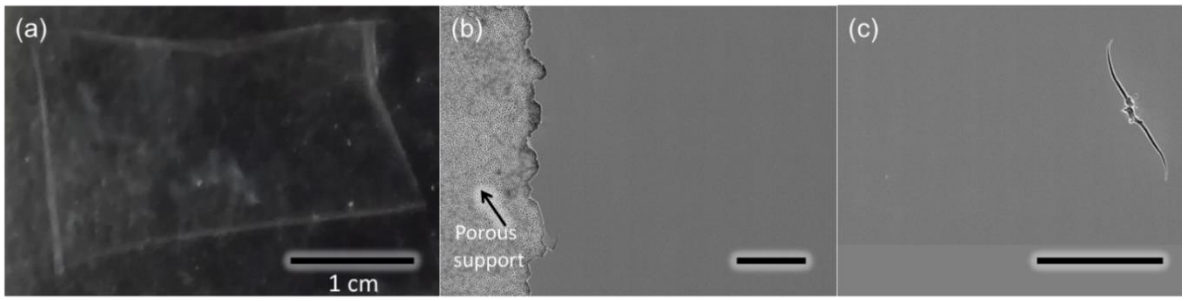

Figure 3-7. (a) Digital image of the PEG-OH/SiO_2 nanomembrane while it was in the detachment solvent. (b,c) SEM image of the nanomembrane transferred onto a porous support. **Scale bar: 10 µm**.

3.3.3 Gas permeation property

Upon testing the gas permeation, the PEG-OH/SiO_2 membrane showed frequent gas leakage problem. Sometimes, cracks were also observed in the nanomembranes by SEM (Figure 3-7c). On the other hand, although not reproducible, the membrane randomly showed CO_2 selective separation behavior over N_2. In situations like this, a caulking layer is applied to alleviate the effects of structural defects.[10] Caulking materials need to have high gas diffusivities, so as not to hinder the performance of the separation layer. Accordingly, a PDMS caulking layer has been coated on PEG-OH/SiO_2 (Figure 3-8) in order to seal the cracks and prevent simple gas leakage.

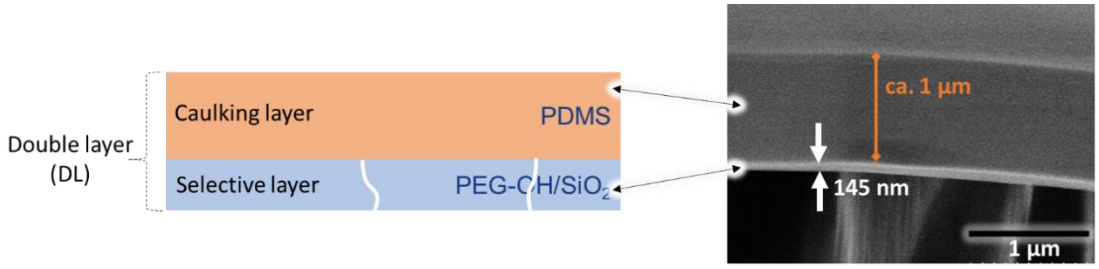

Figure 3-8. Schematics (left) and cross-sectional SEM view (right) of PEG-OH/SiO_2 nanomembrane with PDMS caulking layer.

From the permeance and selectivity results in Table 3-3, the CO_2/N_2 selectivity of (PEG-OH/SiO_2)/PDMS membrane was estimated as ca. 15. This value is higher than the CO_2/N_2 selectivity of pristine PDMS (11.6),[11] signifying that the enhanced selectivity is due to PEG-OH/SiO_2. This is reasonable as the ethylene oxide group in PEG-OH could assist the solubility-selectivity of CO_2 over N_2. However, the improved CO_2/N_2 selectivity was compromised by a decrease in permeance relative to pristine PDMS. This might be because the PEG-OH/SiO_2 layer was very dense and had no molecular pathways. This, in turn, could be attributed to the presence of amorphous SiO_2 in the membrane, as well as the crystalizing nature of PEG[12] that restricts permeation pathways.

Table 3-3. Gas separation properties of pristine PDMS and PEG-OH/SiO_2 with PDMS caulking layer.

Membrane	Permeance, GPU		CO_2/N_2 selectivity
	CO_2	N_2	
Pristine PDMS	3500.00	301.000	11.6
PEG-OH/SiO_2 (with caulking layer)	5.50	0.370	14.8
PEG-OH/SiO_2 layer (Resistance model calculation)	5.52	0.371	14.9

The effect of the caulking layer on gas separation behavior of PEG-OH/SiO_2 was examined by applying the resistance model.[10,13,14] According to the model, the permeance of the double layer (P_{DL}) membrane is related to the permeance of each layer as follows;

$$\frac{1}{P_{DL}} = \frac{1}{P_{PDMS}} + \frac{1}{P_{PS}} \qquad \text{(Eq. 3-3)}$$

where, P_{PDMS} and P_{PS} are the permeances of PDMS caulking layer and PEG-OH/SiO_2 selective layer, respectively.

This relation is valid only when the two layers are free of any defects. The PEG-OH/SiO_2 layer, however, possessed cracks (Figure 3-7c), meaning that small part of the PDMS layer is not in contact with PEG-OH/SiO_2. Therefore, the experimentally measured permeance (P_{meas}) is not equal to P_{DL},[14] but rather they are related as follows.

$$P_{meas} = P_{DL}\frac{A_{PS}}{A_{PDMS}} + P_{PDMS}\left(1 - \frac{A_{PS}}{A_{PDMS}}\right) \qquad \text{(Eq. 3-4)}$$

where, the A_{PS}/A_{PDMS} refers to the area of the PEG-OH/SiO_2 layer covered by PDMS.

It is assumed (based on SEM observation) that the cracks in the PEG-OH/SiO_2 layer constitute about 5% and the rest 95% of the membrane was covered by PDMS. The calculated permeance and selectivity values are listed in Table 3-3. However, there was no significant difference between the experimentally measured and model-based calculated values. This means that the caulking layer has almost no resistance on gas permeation, and the results reflect the behavior of PEG-OH/SiO_2 layer. This, in turn, affirms that the PEG-OH/SiO_2 nanolayer has no serious cracks.

3.4 Discussion

The idea of PEG-OH/TiO_2 blend nanomembranes discussed in this chapter is a follow up of PVA/TiO_2 LBL nanomembrane discussed in Chapter 1 with the aim to find out an alternative preparation route to integrate macroscopic mechanical property with CO_2/N_2 separation function. Two possible ways were considered in order to overcome the low separation performance (where unsatisfactory mechanical stability could be a likely factor) of the PVA/TiO_2 nanomembrane. Using a softer polymer with better gas separation properties, and changing the membrane architecture. Accordingly, a blended type of PEG/TiO_2 FS-NM was developed from a blend formula of a hydroxyl-terminated polyethylene glycol (PEG-OH) and silicon tetraisocyanate. Although no observable mechanical property enhancement was seen, compared to the PVA/TiO_2 membrane, the PEG/SiO_2 hybrid nanomembrane demonstrated improved CO_2/N_2 selectivity.

The obtained results discussed in Chapter 2 and Chapter 3 implied that it is not smooth to improve mechanical property of a nanomembrane while maintaining the separation performance or vice versa only by changing membrane materials. In fact, it could be possible to tune both mechanical property and function of a nanomembrane together. However, this task would be time consuming and costly. Therefore, a more reliable membrane design that comprise fiber-reinforced polymer composites was considered as a preferable approach, and is discussed in Chapter 4.

3.5 Conclusion

Free-standing PEG-OH/SiO_2 blend nanomembrane was prepared by spin-coating. The sol-gel reaction between PEG and $Si(NCO)_4$ was assisted by thermal annealing for improved mechanical property. Because the nanomembrane showed gas leakage due to cracks, PDMS caulking layer has been coated and the gas separation property was estimated by employing the resistance model. Although no significant mechanical property enhancement was observed from physical manipulation, compared to the PVA/TiO_2 LBL nanomembrane discussed in Chapter 2, the PEG-OH/SiO_2 hybrid nanomembrane demonstrated improved CO_2/N_2 selectivity.

References

(1) Koros, W. J. *Macromol. Symp.* **2002**, 188(1), 13-22.

(2) Mersha, A.; Selyanchyn, R.; Fujikawa, S. *CleanE* **2017**, *1* (1), 80–89.

(3) Richardson, J. J.; Bjornmalm, M.; Caruso, F. *Science* **2015**, *348* (6233), 2491.

(4) Vendamme, R.; Onoue, S.-Y.; Nakao, A.; Kunitake, T. *Nat. Mater.* **2006**, *5* (6), 494–501.

(5) Xu, Z. L.; Yu, L. Y.; Han, L. F. *Front. Chem. Eng. China* **2009**, *3* (3), 318–329.

(6) Ye, Y. N.; Frauenlob, M.; Wang, L.; Tsuda, M.; Sun, T. L.; Cui, K.; Takahashi, R.; Zhang, H. J.; Nakajima, T.; Nonoyama, T. *Adv. Funct. Mater.* **2018**, *28* (31), 1801489.

(7) Fei, R.; Means, A. K.; Abraham, A. A.; Locke, A. K.; Coté, G. L.; Grunlan, M. *Macromol. Mater. Eng.* **2016**, *301* (8), 935–943.

(8) Liu, J.; Hou, X.; Park, H. B.; Lin, H. *Chem.Eur. J.* **2016**, *22* (45), 15980–15990.

(9) Takaki, R.; Takemoto, H.; Fujikawa, S.; Toyoki, K. *Colloids Surfaces A Physicochem. Eng. Asp.* **2008**, *321*, 227–232.

(10) Dal-Cin, M. M.; Darcovich, K.; Saimani, S.; Kumar, A. *J. Memb. Sci.* **2010**, *361*, 176–181.

(11) Robb, W. L. *Ann. N. Y. Acad. Sci.* **1968**, *146*, 119–137.

(12) Lin, H.; Freeman, B. D. *Macromolecules* **2006**, *39* (10), 3568–3580.

(13) Henis, J. M. S.; Tripodi, M. K. *J. Memb. Sci.* **1981**, *8* (3), 233–246.

(14) Ai, M.; Shishatskiy, S.; Wind, J.; Zhang, X.; Nottbohm, C. T.; Mellech, N.; Winter, A.; Vieker, H.; Qiu, J.; Dietz, K. J. *Adv. Mater.* **2014**, *26* (21), 3421–3426.

Chapter 4 Mechanical reinforcement of free-standing polymeric nanomembranes via aluminosilicate nanotube scaffolding

Abstract

Owing to their nanometer thickness, large lateral dimensions and self-supporting properties, free-standing nanomembranes (FS-NMs) exhibit outstanding advantages. However, FS-NMs are difficult to manipulate without damage at a macroscopic scale, making mechanical reinforcement still a detrimental challenge for their full exploitation. In this chapter, the development of a new strategy for the preparation of mechanically reinforced sub-100 nm thick free-standing membranes is presented. The key for mechanical toughness of the nanomembrane is the incorporation of very thin (< 15 nm) aluminosilicate nanotube (ASNT) bed scaffold that strengthen the whole composite nanomembrane with polymers. The composite nanomembrane with polydimethylsiloxane (PDMS) demonstrated a 4-fold increase in tensile strength and over 43-times higher biaxial modulus compared to the pristine polymer film. The permselectivity of CO_2 over N_2 affirmed the absence of defects in the ASNT/PDMS nanomembrane. This simple approach could be extended to various polymer materials, including polymers of less film-forming nature. The design concept, fabrication and characterization of the nanomembrane, as well as evaluation of its mechanical properties is discussed.

4.1 Introduction

Free-standing nanomembranes (FS-NMs) have received a rapidly growing interest in a wide range of applications including energy conversion and storage,[1,2] sensing[3,4] and biomedical applications[4] and rarely in molecular separations,[5,6] owing to their nanometer thickness and large lateral dimensions. FS-NMs comprise thicknesses of less than a few hundred nanometers[1] with dual surfaces that can physically separate two spaces,[7,8] by sustaining their size and shape without support.[9,10] FS-NMs offer superlative advantages over their bulk counterparts and other material forms because of the following features: (i) FS-NMs can be transferred onto any substrate of diverse configurations such as planar, curvilinear or wavy structures,[1,4] (ii) they have high lateral size to thickness aspect ratio of greater than 10^6,[7] (iii) FS-NMs have unique interfacial and mechanical properties, including noncovalent adhesiveness and flexibility.[7,11]

Nevertheless, to fully exploit such unique features, FS-NMs need to have sufficient mechanical and chemical stabilities in the macroscopic scale. For example, FS-NMs are expected to enhance mass transport with less energy in separation applications. However, membrane thinning is often encountered by mechanical weakening. Also, excellent mechanical stability of FS-NMs is required in practical applications such as wound-dressing and antibacterial therapeutics[4] where FS-NMs are installed onto uneven surfaces. Therefore, to fully utilize their potential, improving the macroscopic stability of FS-NMs is yet a critical challenge.

Incorporation of inorganic fillers into a polymer matrix[12–14] have been a conventional strategy for synergetic mechanical reinforcement in organic/inorganic composite materials. Yet control of polymer−filler compatibility (such as interfacial interactions) is still a research challenge for the development of chemically stable and defect-free membranes.[12] In addition, molecular level designs such as organic/inorganic interpenetrating networks,[15] double-network hydrogels[16] and layer-by-layer assembly[10,17] could be used to prepare mechanically enhanced nano and micro-thick membranes. However, such procedures often require materials to satisfy both the properties of membrane formation ability and functional moieties in a membrane, resulting in the limitation of material selection.

Previous reports also demonstrated the deposition of thin polymeric membranes on top of porous supports via interfacial polymerization.[18,19] Rigid materials with micro-scale thickness are often used as supports. For example, Livingston's group develops several solvent nanofiltration

membranes with thicknesses down to a few tens nm via *in situ* interfacial polymerization on crosslinked polyimide and other porous supports.[18,20] Also, Droudian et al, reported the preparation of polyamide and imide nanofilms around CNT buckypaper at vapor-liquid interface.[19] However, this approach comes with critical requirements of the porous support. The support needs to have very smooth surface with certain functional moieties to allow the deposition of uniform and defect free separation layer. This technique is also restricted by the range of polymer selection, partly because it requires the polymer material to have specific interactions with the support layer. This implies that a more reliable and versatile method is still desirable.

Thus, a new strategy employing aluminosilicate nanotube (ASNT) networks as bed scaffolds to deposit freestanding polymeric nanofilms is presented. Polydimethylsiloxane (PDMS) was taken as a starting polymer since it is commonly used as a gas separation membrane material. Acting as a strong backbone, ASNT networks strengthen the polymer nanomembrane. ASNTs ($Al_2O_3.SiO_2.2H_2O$) are synthetic analogues of natural imogolite which was first discovered in volcanic soils in Japan.[21,22] They are metal oxide-based inorganic materials, with remarkable 1D tubular nanostructures of internal and external diameters of about 1 and 2.5 nm, respectively (Figure 4-1).[23]

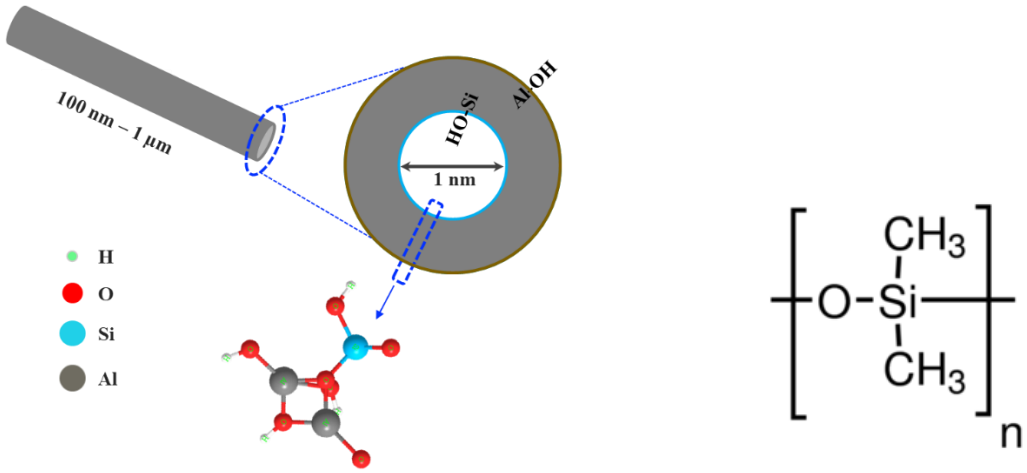

Figure 4-1. Structure of aluminosilicate nanotube (left) and polydimethylsiloxane (right)

The choice of ASNTs is mainly based on two structural features. (i) To utilize its reactive hydroxyl functionalized surfaces in order to make crosslinked nanofiber backbones for high mechanical reinforcement. For example, the characteristic OH-functionalized surfaces allow sol-gel reaction with metal oxides.[24] Such surfaces also facilitate excellent solution processability and good

adhesion with polymers.[25] (ii) In addition to the above merits, ASNTs have one-dimensional structure and thus high aspect ratio[25], which facilitates multiple hydrogen bonding that further enhances the mechanical property of the scaffold. These properties are advantageous than the inert chemical nature of other nanotubular materials such as carbon nanotubes (CNTs). Although CNTs are the most widely used nanotubular materials in membrane-based separations[26] and other applications,[27] harsh surface modifications are often required to improve their solution dispersibility and interaction with polymers.[12] Aggressive treatments alter CNT integrity and properties.[27] Also, energy intensive and extreme synthesis conditions restrict the scope of their application.[12] Furthermore, as reflected by the Young's modulus of ASNTs (280 GPa)[28] and CNTs (~ 1 TPa),[29] the relative softness of ASNTs is complementary to develop flexible fiber reinforced composite membranes.

In this chapter, a new type of simple and inexpensive method has been introduced for the preparation of tough free-standing polymeric nanomembranes via scaffolding with crosslinked nanofibrous networks. This approach allows (i) to transfer the composite nanomembrane onto any arbitrary substrate for a desired application since the nanomembrane is prepared independently of its utilization platform, (ii) simple deposition of multitude of polymer nanofilms with tailor made functionalities by spin-coating, (iii) to maintain macroscopic stability since mechanical stress on the soft polymer component can be transferred to the inorganic nanofiber scaffold which is embedded into the polymer film on one side of the composite nanomembrane.

4.2 Experimental

4.2.1 Materials

Silicon wafer with a 350 µm thickness and glass substrate were used as substrates. Poly(4-vinylphenol) (PVP, M_w=11000, Sigma-Aldrich) was used as sacrificial layer. $AlCl_3.6H_2O$, NaOH, HCl and acetic acid (HAc) were purchased from Wako Co., Ltd. and used to synthesize ASNTs. Tetraethyl orthosilicate (TEOS, Sigma-Aldrich) was also used in the synthesis of ASNTs. LAQUA pH/Ion/Cond/ meter (F-74, Horiba Scientific) and digital thermometer (Sato Chemical Co., Ltd) were also used to monitor the pH and temperature of the synthesis process. Titanium *n*-butoxide ($Ti(O^nBu)_4$, Gelest Inc.) was used as TiO_2 precursor. Polydimethylsiloxane (PDMS, Sylgard® 184) was the polymer precursor. Ethanol, chloroform and n-hexane were purchased from Wako Co., Ltd. and used as received. Deionized water (18.3 MΩ cm^{-1}, Millipore, Direct-QTM) was used for rinsing and solution preparation.

4.2.2 Synthesis of ASNTs

ASNTs were synthesized based on a modified reported method.[30] It involves simple and inexpensive hydrothermal condensation of dilute concentrations of tetraethyl orthosilicate (TEOS, Kanto Chemical) and $AlCl_3.6H_2O$ (Wako Ltd.) at 95 ^oC for 96 hours. The surface morphology and Al/Si ratio of the nanotubes were studied by transmission electron microscopy (TEM) and scanning electron microscope-electron diffraction spectroscopy (SEM-EDS) respectively.

4.2.3 Nanomembrane preparation procedure

The overall nanomembrane preparation process is illustrated schematically in Figure 4-2. In the preliminary step, a cleaned glass substrate was treated by oxygen plasma etching to hydrophilize its surface. Details of the substrate cleaning and oxygen plasma treatment are outlined in Chapter 2, Section 2.2.2. A sacrificial polymer substrate of PVP was then spin-coated (3000 rpm, 60 s) from 15 wt% ethanol (EtOH) solution and annealed at 120^oC for 5 minutes.

Subsequently, the as-synthesized aqueous dispersion of ASNTs (~ 0.3 mg/ml) was deposited on the sacrificial layer by carefully optimized spin-coating condition. Here, spin-coating condition was essential for uniform deposition of ASNTs. Thus, spinning speed was ramped up from 500 rpm (held for10 s) to 1500 rpm (for 30 s) and finally to 3000 rpm (for 30 s). The deposited ASNT network was allowed to dry in ambient air for 15 min.

Afterwards, a dilute chloroform solution of 1 mM $Ti(O^nBu)_4$ was spin-coated (3000 rpm, 60 s) and left in an ambient air for 15 min to undergo hydrolysis and condensation. The deposited TiO_2 wrap the surface of the ASNTs, and thereby crosslink them each other. The alternate coating of ASNTs and TiO_2 was repeated until the desired cycle.

Finally, a hexane solution of PDMS was prepared from Sylgard® 184 kit by mixing 10 parts of the pre-polymer base (part A) to 1 part of the curing agent (part B) based on the manufacturer's recommendation,[31] and spin-coated at a speed of 4000 rpm for 180 s. It was then crosslinked at 80ºC for 12 hours.

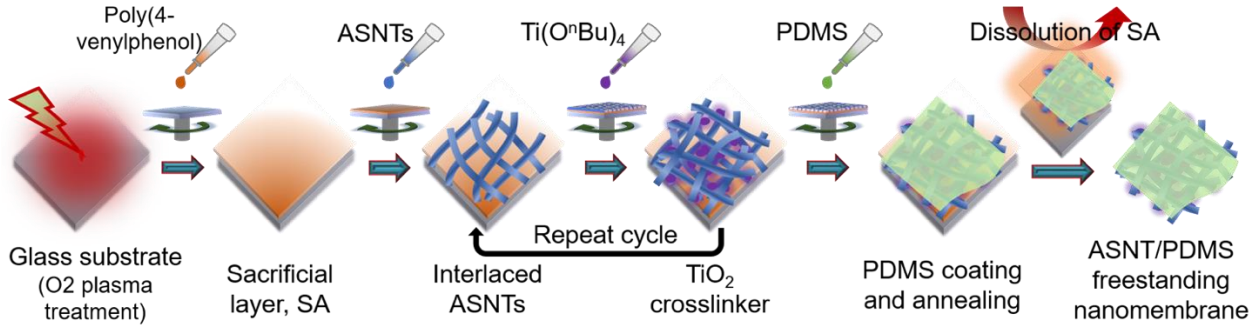

Figure 4-2. Schematic illustration of nanomembrane preparation procedure.

Once coating was completed, the composite film on the glass substrate was framed by Kapton tape or silicon rubber ring and immersed in EtOH to dissolve the sacrificial layer. This step detaches the self-supporting nanomembrane, leaving it suspended in the sub-surface of the solution.

FS-NMs of the general designation $(A\text{-}T)_n$/PDMS (where A = ASNTs, T = TiO_2, n = number of cycles of alternate ASNTs and TiO_2 coating) were fabricated by spin-coating. A similar procedure was followed to prepare A_n/PDMS and T_n/PDMS, except that TiO_2 was absent in the case of A_n/PDMS and ASNT was absent in the case of T_n/PDMS. To avoid confusion, the types of nanomembranes prepared and the materials used are summarized in Figure 4-3.

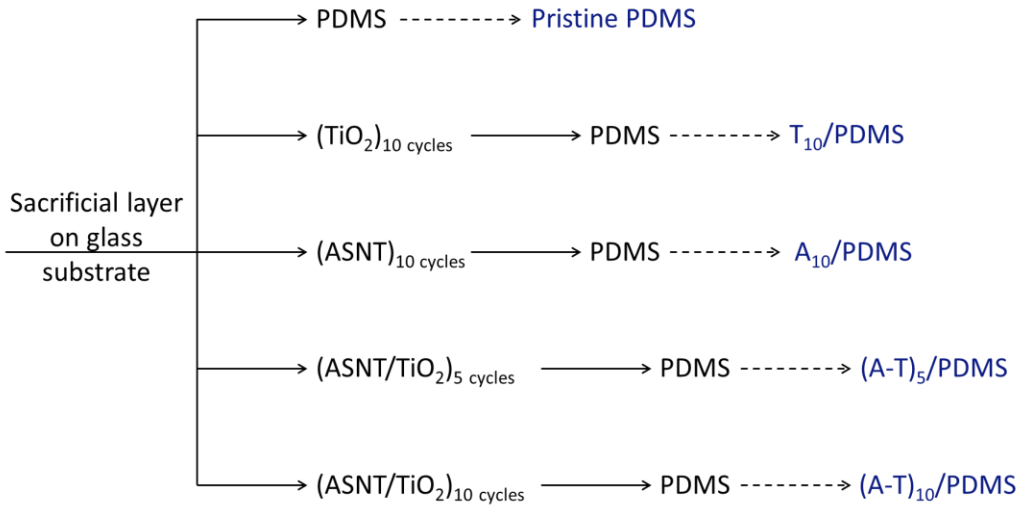

Figure 4-3. Scheme of nanomembrane preparation, showing the constituent materials and the final membrane (after dotted arrow).

4.2.4 Membrane characterization

The morphological changes during the membrane preparation process, as well as the membrane thickness were examined by field emission scanning electron microscope (FE-SEM, Hitachi S-5200). Additionally, the chemical environment and composition of Si, Al and Ti in the vertical structure of the membranes were analyzed by x-ray photoelectron spectroscopy (PHI 5000 Versa Probe II). Specimen for XPS analysis were prepared on a substrate that do not contain any of the target elements (Al, Si, Ti). Thus, for $(A\text{-}T)_{10}$/PDMS composite nanomembrane, the FS-NM was transferred onto polycarbonate (VCTP02500, Isopore^{TM}) porous substrate. In the case of pristine ASNT film, specimen was prepared by vacuum filtration of ASNT aqueous dispersion on the polycarbonate filter. In addition, polycarbonate substrate was measured as a blank along with the membranes.

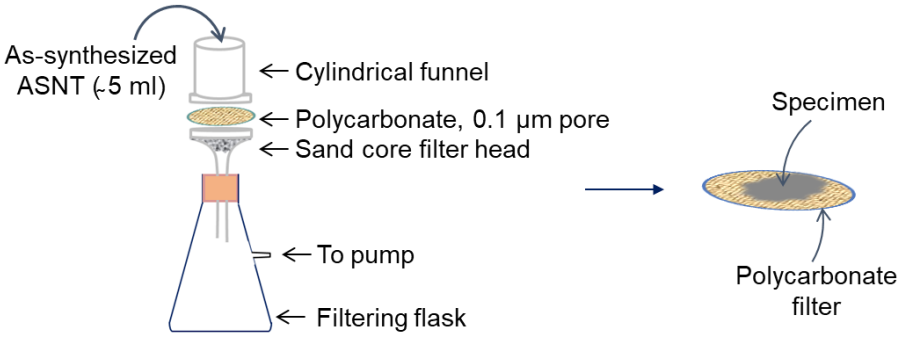

Figure 4-4. Schematics of ASNTs film preparation for XPS analysis.

4.2.5 Investigation of mechanical properties

Mechanical properties of the nanomembranes were evaluated by bulging test,[6,32,33] a well-known technique to determine quantitatively the mechanical properties of supported and freely suspended thin films. In this work, hydraulic bulge test in which liquids are used as a mechanical stress was employed. Care should be taken in selecting an appropriate liquid that is stable, and at the same time, does not interact with the membrane under investigation. Thus, distilled water was used as a source of pressure exerted on nanomembranes since it doesn't have any swelling effect on PDMS.[34]

4.2.6 Gas permeation experiment

Gas permeation was measured by a commercial instrument (GTR-11A/31A system, GTR Tec Corp., Japan) coupled to gas chromatography, and the overall experimental setup is illustrated schematically in Chapter 2, Figure 2-3. An 80:20 N_2/CO_2 mixture gas was allowed to pass through the membranes at a total pressure difference of 200 kPa. The pressure of the feed gas was set at 100 kPa as a gauge pressure, whilst the permeate side was maintained in vacuum condition. Measurements were made at room temperature. The volume of gas passed through the membrane per unit time was measured by gas chromatography. Then, gas permeance and separation factor were calculated according to Equations 2-1 and 2-2, respectively.

4.3 Results and discussion

4.3.1 ASNT synthesis and characterization

ASNTs were synthesized by hydrothermal condensation of $AlCl_3.6H_2O$ and TEOS at 95 ºC following a modified Farmer's method.[30] The synthesis process is summarized schematically in Figure 4-5. Factors that need to be considered during the process include ultra-dilute concentrations (a few millimolar) of reactants, ratio of reactants, slow rate of mixing (dropwise), continuous and vigorous stirring, pH control and refluxing temperature. pH control is the most crucial parameter in the synthesis process, mainly because a medium above pH 5 causes aggregation of precursors that halts the formation of nanotubes, and would rather lead to amorphous oxides.

On the basis of a previous report,[35] the synthesis procedure and growth phenomenon of ASNTs is highlighted as follows. Initially, Al and Si precursor solutions were mixed in the Al/Si ratio of 1.8; pH of the solution was about 3.8. After stirring the mixture for about an hour, pH was ramped up to 5 by slow addition of 0.1 M NaOH (300 µl/min). Ramping up pH allows co-condensation of the precursors to form aluminosilicate precursor. When pH reached 5, it was immediately decreased to 4.5 by adding a mixture of 0.1 M HCl and 0.2 M HAc. At pH 5, nanoparticle condensates (aluminosilicate precursors) form, and then disappear upon re-acidification to pH 4.5. This step prevents simple precipitation of amorphous materials. Afterwards, it was stirred for about 2 hrs and heated under reflux at 95 ºC for 96 hrs. During the heating process, the nanoparticulate precursors self-assemble to form nanorings, and eventually grow into nanotubes.[36]

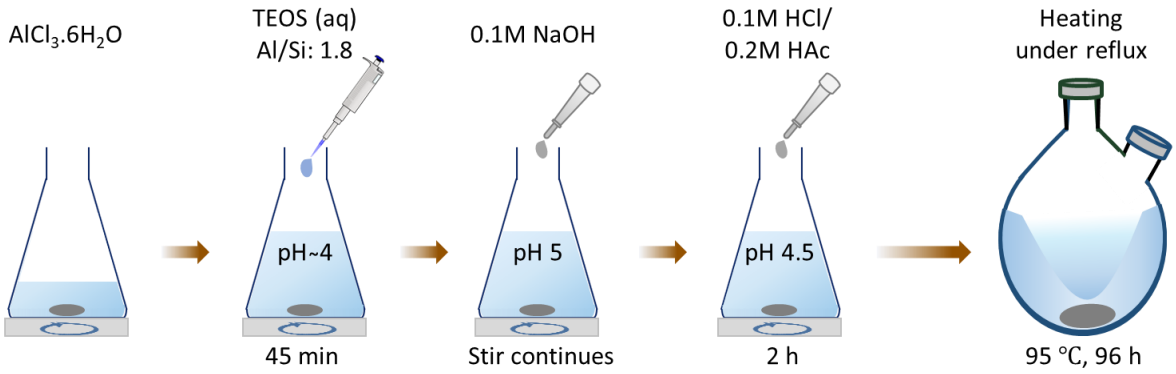

Figure 4-5. Schematic representation of the ASNT synthesis process.

The formation of the ASNTs and the Al/Si ratio in the synthesized nanotubes were confirmed by TEM (Figure 4-6a) and SEM-EDS (Figure 4-6b). The length of the ASNTs at 96 hrs of synthesis time was estimated as less than 1 µm. However, the length of ASNT bundles in the specimen film is about a few micrometers. From membrane preparation perspective, a synthesis time of 72–120 hrs was required to obtain ASNTs with lengths that can readily form interlace structure.

The Al/Si ratio obtained from SEM-EDS is comparable to the ratio of the corresponding reactants added for synthesis. The Pt peak in the EDS spectra is because the specimen was sputtered by Pt for SEM observation.

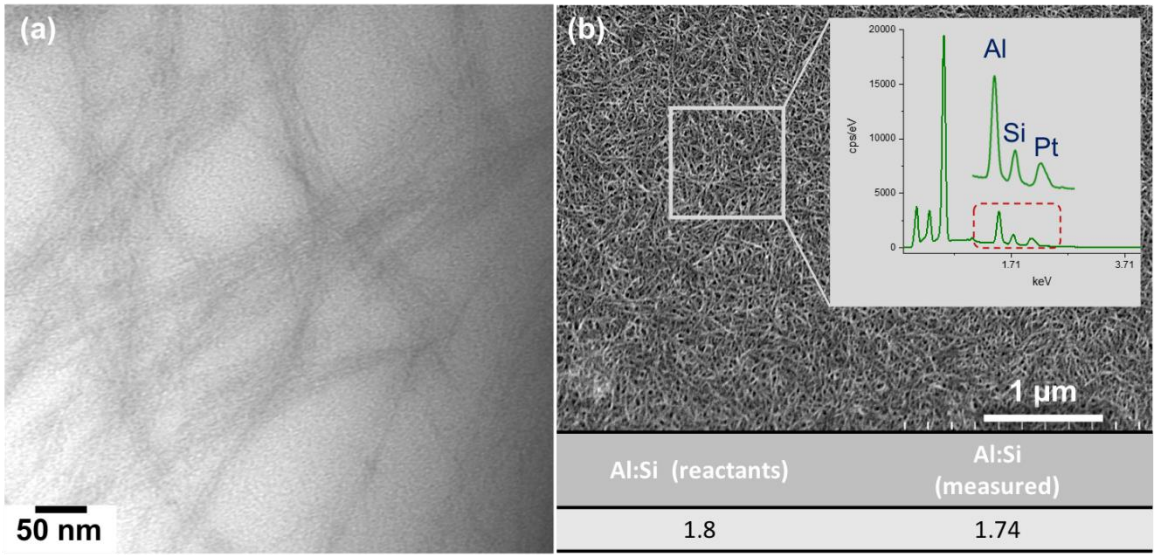

Figure 4-6. TEM micrograph of synthesized ASNT bundles (left) and Al/Si ratio in the synthesized ASNTs determined by scanning electron microscope-electron diffraction spectroscopy (SEM-EDS).

4.3.2 Nanomembrane design

The present membrane design was inspired by the cytoskeleton in biological membranes. It involves use of ASNT scaffolds to strengthen polymeric nanomembranes. Basically, the concept is based on the traditional mechanical reinforcement by compositing organic and inorganic materials. However, in this study, the concept was advanced a step forward into a more mechanically sound architecture by creating bed-like inorganic nanofiber backbones to scaffold ultrathin polymer coatings as depicted schematically in Figure 4-7. Such architecture could benefit in two ways. (i) The nanofiber network brought about significant mechanical reinforcement in

spite of constituting only a very small portion (ca. 15%) of the overall FS-NM thickness. (ii) It also assists nanofilm formation ability of polymers which are often difficult to span into defect free FS-NMs.

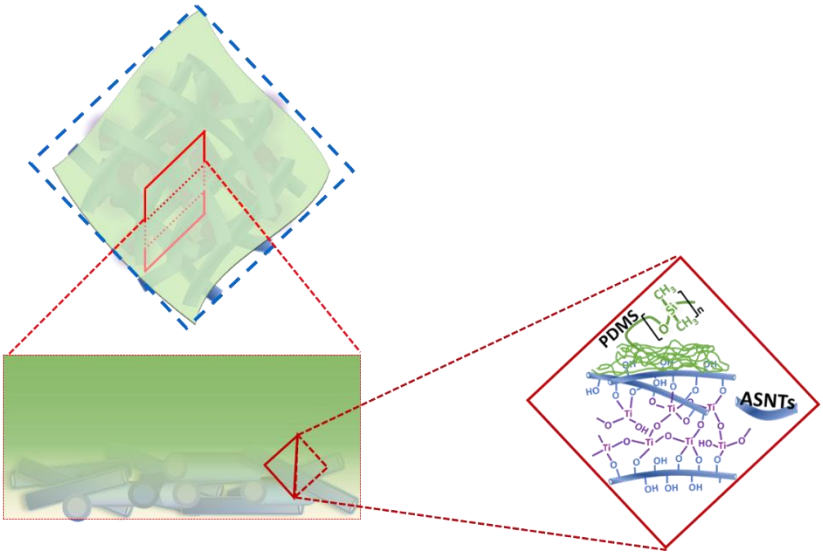

Figure 4-7. Schematic representation of $(A\text{-}T)_{10}$/PDMS nanomembrane depicting the TiO_2-crosslinked ASNTs and the PDMS top layer.

4.3.3 Nanomembrane preparation, morphology and structural analysis

4.3.3.1 Scaffold preparation

At first, a randomly interlaced ASNTs network (Figure 4-8a) was deposited on the sacrificial layer from an aqueous dispersion of the synthesized ASNTs. Here, spin-coating condition was essential for uniform ASNTs deposition. Spinning speed was ramped up from 500 rpm (held for10 s) to 1500 rpm (for 30 s) and finally to 3000 rpm (for 30 s).

The ASNT bundle structures (Figure 4-8b) formed during spin-coating contribute positively to the mechanical enhancement of the scaffold. The mechanical stability was further improved by TiO_2 crosslinking. Upon coating titanium n-butoxide, it reacts with surface hydroxyl groups of ASNTs via sol-gel reaction[24] as illustrated schematically in Figure 4-7, wrapping ASNTs with a thin layer of TiO_2. The alternate spin-coating of ASNTs and TiO_2 was repeated until the desired cycle. The thickness of $(A\text{-}T)_{10}$ was only about 14 nm on the sacrificial layer (Figure 4-8e).

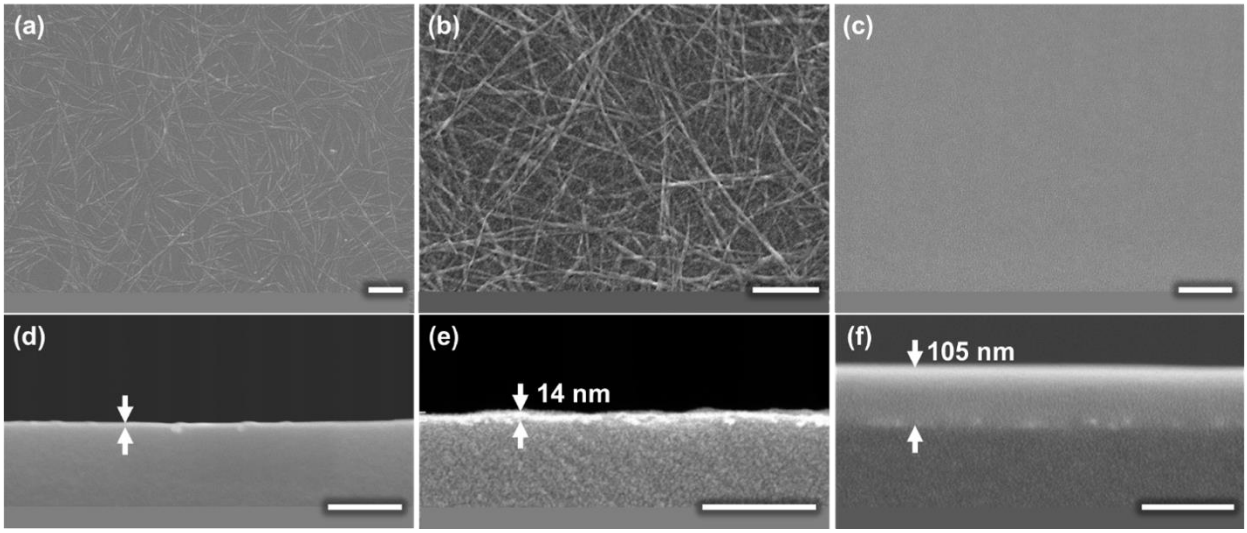

Figure 4-8. SEM observation of morphological changes during the nanomembrane preparation process, **Scale bar: 200 nm**. (a) Bare ASNTs. (b) Crosslinked ASNTs network structure after 10 cycles of alternate ASNT and TiO_2 coating steps, i.e., $(A\text{-}T)_{10}$. (c) Film surface became smooth following PDMS coating on (b), i.e., $(A\text{-}T)_{10}$/PDMS. (d-f) Cross-sectional view of (a), (b) and (c) respectively. All images were recorded on PVP sacrificial layer before membrane detachment.

Distinct layer of TiO_2 was not formed on top of the ASNT network as confirmed by SEM observation (Figure 4-8b,e). However, the presence of TiO_2 demonstrated an apparent change in the mechanical stability of ASNT networks. The effect of TiO_2 was investigated by preparing two separate films on a sacrificial layer. (i) ten cycles of ASNTs with no TiO_2 involved and (ii) ten cycles of alternate ASNT/TiO_2. In the absence of TiO_2 (Case i), the repeatedly coated ASNTs were unstable and fragmented into small pieces that are not visible to naked eye when the film was immersed in EtOH for detachment. On the other hand, the $(A\text{-}T)_{10}$ film (Case ii) remained stable in the detachment solvent even though it was broken into millimeter-scale flakes. Despite its ultrathinness, the $(A\text{-}T)_{10}$ flakes could be transferred onto porous alumina for SEM observation (Figure 4-9). Also, the $(A\text{-}T)_{10}$ scaffold was not very rigid (Figure 4-9a). It, however, has cracks introduced during physical manipulation (Figure 4-9b). Although direct confirmation of Al—O—Ti bond formation was difficult, the ASNTs were assumed to be crosslinked by TiO_2 based on the XPS elemental analysis (where Al, Ti and Si were detected on the ASNT side of the membrane) and nature of the surface sol-gel reaction.[24] Significant improvement in mechanical stability is also additional evidence for the existence of crosslinking. The presence of TiO_2 could also suppress large ASNT aggregate formation during repeated spin-coating.

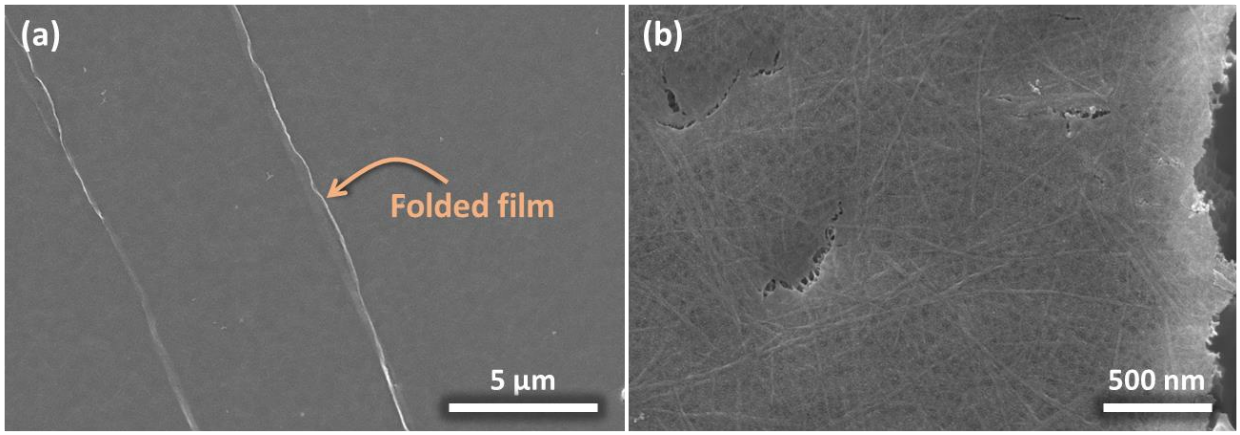

Figure 4-9. SEM image of $(ASNT/TiO_2)_{10}$ film transferred onto porous alumina support.

4.3.3.2 Polymer coating

Once the $(A\text{-}T)_{10}$ scaffold was prepared, the PDMS precursor was coated and crosslinked at 80ºC *in-situ* on the surface of ASNT scaffold layer. The film surface turned smooth (Figure 4-8c). As can be seen in the cross-sectional image (Figure 4-8f), no boundary was seen between PDMS and $(A\text{-}T)_{10}$ network layer. PDMS was embedded into the nanofiber network structure and filled the space between the ASNTs, resulting in a fused structure.

The penetration of PDMS into the ASNT network structure was further studied by XPS elemental analysis on both sides (ASNT side and PDMS side) of the detached $(A\text{-}T)_{10}$/PDMS membrane. Two parameters were considered for comparison; (i) Al/Si ratio and (ii) Chemical environment of Si atom. The results are summarized in Table 4-1 and Figure 4-10. Here, it is worth considering that the approximate electron mean free path (depth of electron extraction) in XPS is 2–10 nm,[37] which is close to the thickness of ASNT network structure of $(A\text{-}T)_{10}$/PDMS. Thus, I assume that the obtained data in the vicinity of both sides of the membrane reflects concentration of elements within 15 nm thickness.

As can be seen in Table 1, the Al/Si ratio on the ASNT side of the $(A\text{-}T)_{10}$/PDMS was far smaller than that of pristine ASNT film (also see Figure 4-10b), implying that additional Si was present in the vicinity of ASNT side of the membrane. The additional Si should come from the PDMS interpenetrated into the ASNT network layer. This is one evidence that PDMS was embedded into the ASNT-scaffold structure.

Table 4-1. Al/Si ratio in pristine ASNT and ASNT side of $(A\text{-}T)_{10}$/PDMS.

Membrane	Al/Si ratio*[a]	Comment
Pristine ASNT film	1.3	Reference for comparison*[b]
ASNT side of $(A\text{-}T)_{10}$/PDMS	0.05	Ti was also detected (Figure 4-10c)
PDMS side of $(A\text{-}T)_{10}$/PDMS	—	No Al and Ti were detected (Figure 4-10a,c)

*[a]Ratio is calculated from the corresponding peak areas.

*[b]The Al/Si ratio of 1.3 was used as a reference for comparison. However, this value deviates from the stoichiometric ratio (1.8), as well as that determined experimentally by SEM-EDS (Figure 4-6). This deviation could be due to impurities (most probably unreacted Al-Si precursors in disproportional quantity).

Furthermore, the chemical environment of Si was investigated via deconvolution of Si2p peaks to confirm if the excess Si on the ASNT-side of the membrane was from PDMS itself. The Si in ASNTs is in the form of silica and has a $Si(\text{-}O)_4$ binding environment, located at 103.0 ± 0.2 eV.[38] Whereas, the Si in PDMS has a $Si(\text{-}O)_2$ environment (Figure 4-10f) at a binding energy of 102.0 ± 0.1 ev.[39] Therefore, from XPS analysis data on the ASNT-side of $(A\text{-}T)_{10}$/PDMS (Figure 4-10d), the smaller peak at ~ 102.1 eV could be assigned to the $Si(\text{-}O)_2$ component peak and corresponds to PDMS, indicating that portion of the PDMS reached the vicinity of the ASNT network side of $(A\text{-}T)_{10}$/PDMS membrane.

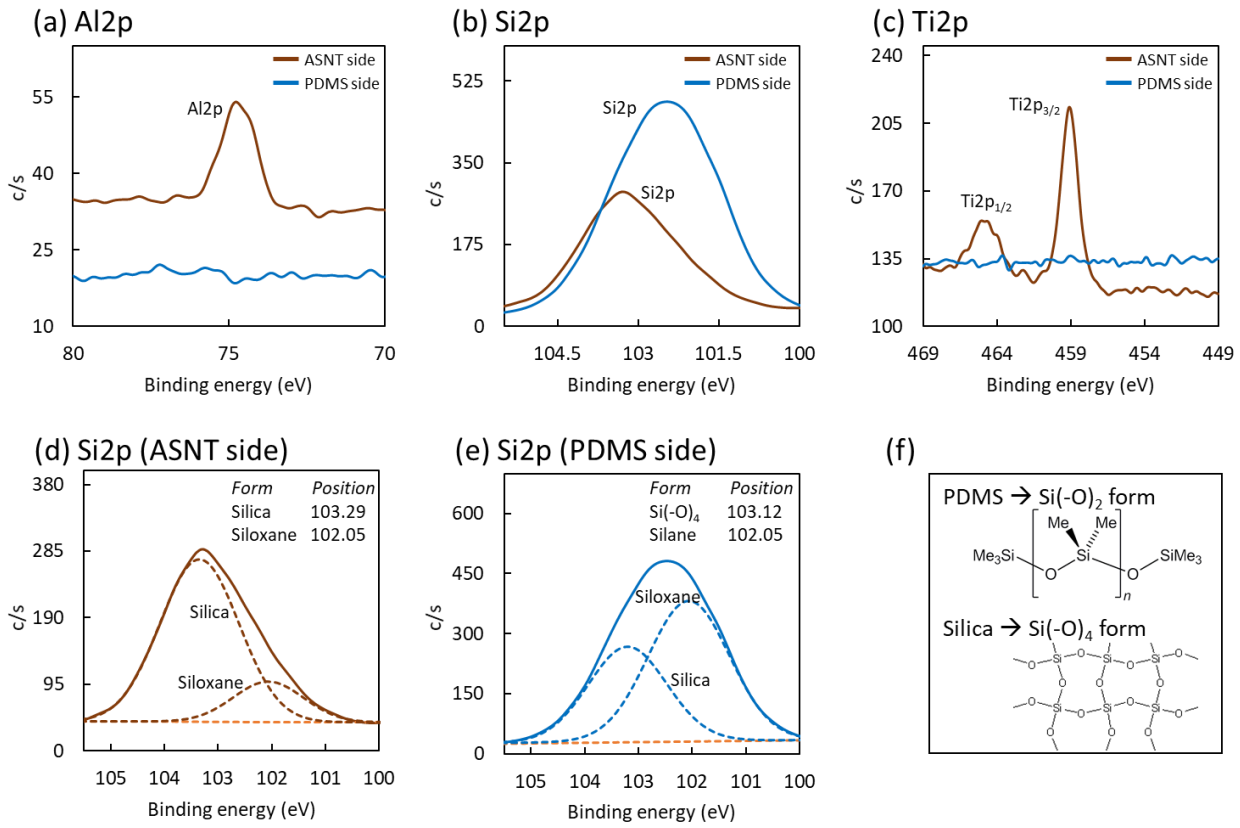

Figure 4-10. (a-e) XPS elemental analysis of both sides of the $(A\text{-}T)_{10}$/PDMS nanomembrane. (f) Structures of PDMS and silica network depicting the Si binding environments.

It was also interesting that the quantity of siloxane form of Si on ASNT side was smaller than that of PDMS side (Figure 4-10e). This signifies that only small portion of PDMS could penetrate into the ASNT network structure.

FS-NMs of various thicknesses were prepared from different concentrations of PDMS ranged from 1.3 wt% to 0.6 wt% (Figure 4-11). The concentration of PDMS was selected aiming to prepare nanomembranes down to sub-100 nm thicknesses while ensuring their mechanical robustness.

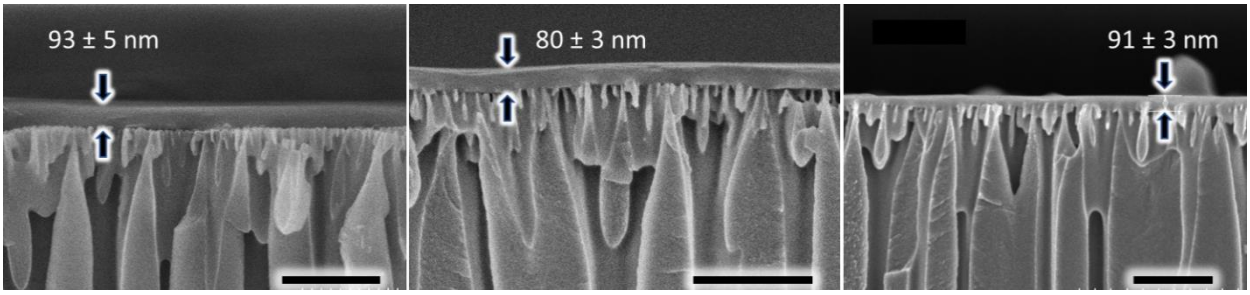

Figure 4-11. Thickness of nanomembranes determined by SEM after being transferred onto porous alumina. (a) $(A\text{-}T)_{10}$/PDMS with PDMS concentration of 1.3 wt%. (b) $(A\text{-}T)_{10}$/PDMS with PDMS concentration of 0.6 wt%. (c) pristine PDMS (0.9 wt%). **Scale bar: 500 nm**.

4.3.4 Investigation of mechanical properties

4.3.4.1 Physical manipulation

Mechanical robustness of the prepared FS-NMs was, in part, demonstrated by simple lift off process from the membrane detachment solvent. Once detached by dissolving the sacrificial layer in EtOH (Figure 4-12a), the composite nanomembrane with Kapton frame could be lifted off by simply holding it with a tweezer (Figure 4-12b) with almost zero failure rate. A large size (as high as 40 mm diameter) and ultrathin (as low as 65 nm) nanomembranes could be picked up and manipulated in air without any damage, revealing excellent macroscopic mechanical stability. In contrast, lifting off of pristine PDMS nanomembrane with comparable thickness was difficult, and has high failure rate (~50%). Similar observation was made by Khang et al,[40] claiming less than 50% success rate in the transfer of PDMS nanomembranes thinner than 100 nm. The enhanced mechanical stability in the macroscopic manipulation of the $(A\text{-}T)_{10}$/PDMS nanomembrane is ascribed to the presence of crosslinked scaffolding. This property ensures stable handling of the nanomembranes for practical use. The composite nanomembranes were also transparent (Figure 4-12c) like pristine PDMS, and smooth.

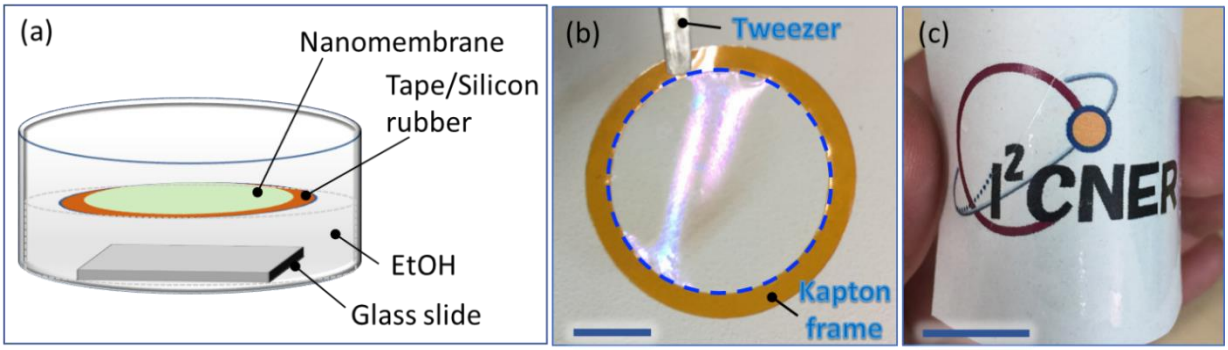

Figure 4-12. (a) Schematic representation of the membrane detachment process. (b,c) Digital images of detached nanomembranes, **Scale bar: 1 cm**; (b) nanomembrane lifted off by a tweezer and dried in air (color is due to reflection of light). (c) Nanomembrane transferred onto a printed text.

4.3.4.2 Bulging test

In addition to physical manipulation, quantitative evaluation of mechanical properties was also conducted by hydraulic bulging test depicted by the apparatus in Figure 4-13c. FS-NMs were suspended onto the bottom of the cylindrical funnel (hereafter referred to as glass tube) and affixed by a Kapton tape as illustrated schematically in Figure 4-13b. The digital photo of the affixed nanomembrane ready for bulging test is shown in Figure 4-13c. Distilled water was continuously loaded dropwise onto the nanomembrane surface inside the tube; the corresponding membrane deflection was recorded by a video camera, which was set perpendicular to the deflection direction.

To avoid error in the measurement of deflection height, the stiffness of the tape was confirmed by a control test. Meaning that water was loaded directly on the tape inside the tube and its resistance to deflection was checked. The tape was so stiff that it doesn't show any deflection up to 16 g water loading (which was twice the maximum load hold by the nanomembrane).

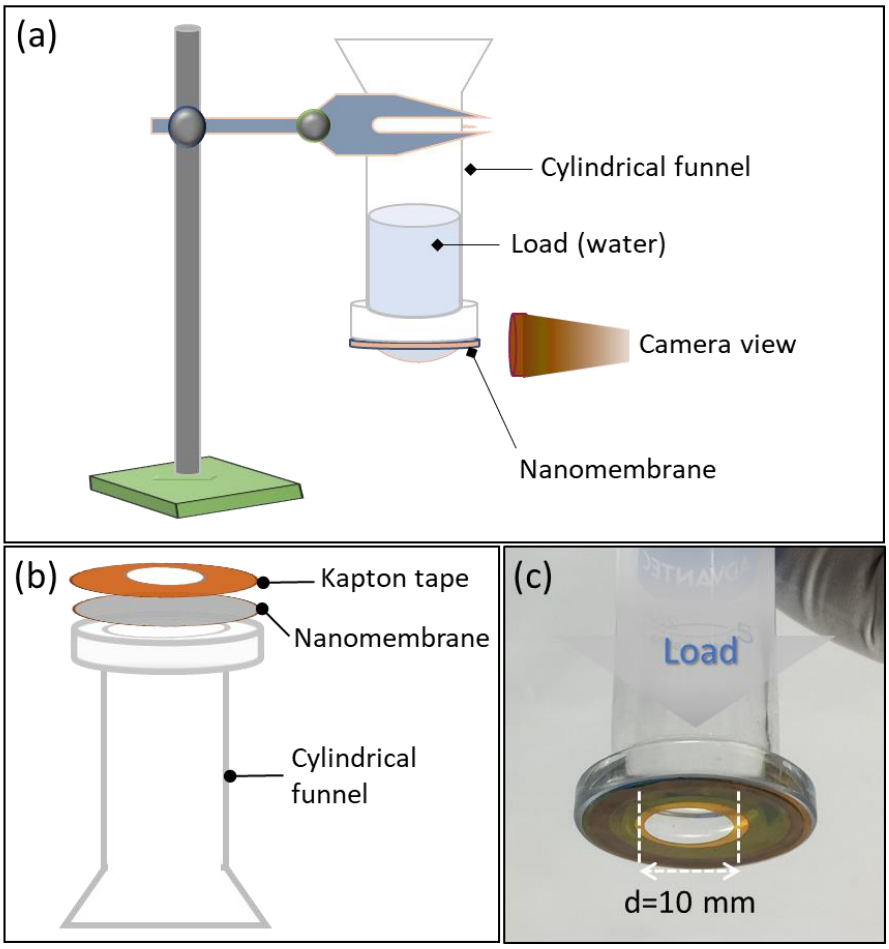

Figure 4-13. Schematic diagram of (a) membrane assembly for bulging test; (b) hydraulic bulging test apparatus. (c) Digital image of the nanomembrane assembled to the base of a cylindrical funnel by Kapton tape for bulging test (*Light gray* area between the dashed lines indicates membrane exposed for loading; *orange circle:* membrane covered by Kapton tape; the *rest* of the area refers membrane sandwiched between the glass tube and the tape).

The deflection of nanomembranes due to applied pressure (Figure 4-14) was used to calculate stress, strain and biaxial modulus according to the following equations;[32,33]

$$\text{Stress, } \sigma = \frac{P(a^2+d^2)}{4td} \qquad \text{(Eq. 4-1)}$$

$$\text{Strain, } \varepsilon = \frac{S-S_0}{S_0} \qquad \text{(Eq. 4-2)}$$

$$\text{Biaxial modulus, } Y = \frac{3Pa^4}{8td^3} \qquad \text{(Eq. 4-3)}$$

where P is the applied pressure, a is the radius of active nanomembrane, t is nanomembrane thickness determined by SEM, d is deflection of the nanomembrane, and S and S_0 are final and initial lengths of the curve in Figure 4-14.

When considering the effect of elastic constants on the accuracy of spherical membrane equations,[32] the actual biaxial modulus can be described simply as;

$$Y_{act} = \frac{Y_{cal}}{1-0.241v} \qquad \text{(Eq. 4-4)}$$

where v is the Poisson's ratio and a value of 0.3 is assumed in all calculations. This assumption is based on previous reports that the addition of fibers or elastic rods leads to a monotonic evolution of Poisson's ratio toward the value 0.25–0.3 either from above or below.[41]

The nanomembrane deflection and curve lengths were determined by processing the captured images in ImageJ software. Similarly, the ultimate elongation and the ultimate tensile strength (UTS) were calculated from the maximum deflection at the rupture pressure.

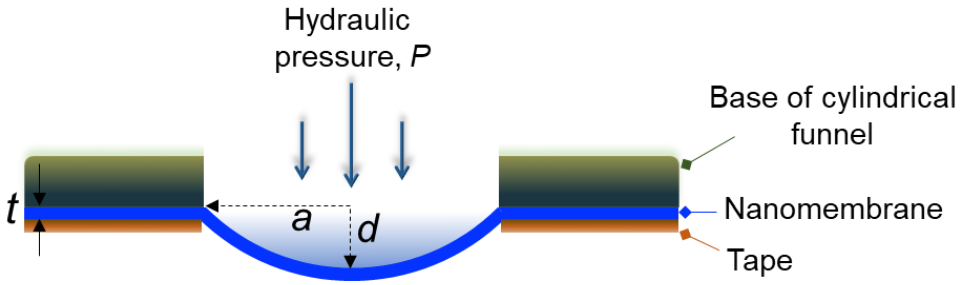

Figure 4-14. Schematic description of membrane bulging against applied pressure; t=nanomembrane thickness, a=radius, d=deflection.

Nanomembranes responded differently to the applied equal hydraulic pressure of 312.1 Pa, which is equivalent to 2.5 grams of load (Figure 4-15a). I prepared a series of nanomembranes of comparable thickness (within 80–95 nm) to study the contribution of each constituting membrane material for the mechanical property enhancement; Pristine PDMS, T_{10}/PDMS, A_{10}/PDMS, $(A\text{-}T)_5$/PDMS and $(A\text{-}T)_{10}$/PDMS. It is assumed that a small difference in thickness has insignificant effect on the mechanical property of the composite nanomembrane. A membrane thickness of 90 nm was employed in all the calculations.

Table 4-2. Summary of thickness (measured by SEM) and mechanical property results of the prepared nanomembranes.

Nanomembrane	Maximum load, g	Deflection, mm	Ultimate tensile strength, UTS	Biaxial modulus, Y
PDMS	2.50±0.13	0.636±0.017	8.92±0.057	3.40±0.26
T_{10}/PDMS	2.47±0.71	0.593±0.021	8.69±0.051	4.03±0.42
A_{10}/PDMS	3.58±0.65	0.344±0.010	13.00±0.135	31.16±3.04
$(A\text{-}T)_5$/PDMS	4.00±0.62	0.318±0.250	15.37±0.522	44.86±10.80
$(A\text{-}T)_{10}$/PDMS	7.98±0.36	0.250±0.010	34.64±0.647	172.60±18.22

Pristine PDMS membrane demonstrated the highest deflection height, followed by titania scaffolded PDMS with only small decrease in height (Figure 4-15a_1, a_2). An apparently lower deflection was observed in ASNT-scaffolded PDMS (Figure 4-15a_3) compared to TiO_2-supported and pristine PDMS nanomembranes. This is due to the presence of nanofiber networks in A_{10}/PDMS. Even if they are not crosslinked by TiO_2, the hydrogen bonding-reinforced ASNT interlaced structure in the A_{10}/PDMS improved its stiffness. When the ASNTs were crosslinked by TiO_2 via sol-gel reaction, as in $(A\text{-}T)_5$/PDMS and $(A\text{-}T)_{10}$/PDMS, the mechanical property of the nanofiber scaffold layer was significantly enhanced, which ultimately reinforced the composite nanomembrane. This phenomenon was reflected by the corresponding minimal deflection of the nanomembranes (Figure 4-15a_4, a_5).

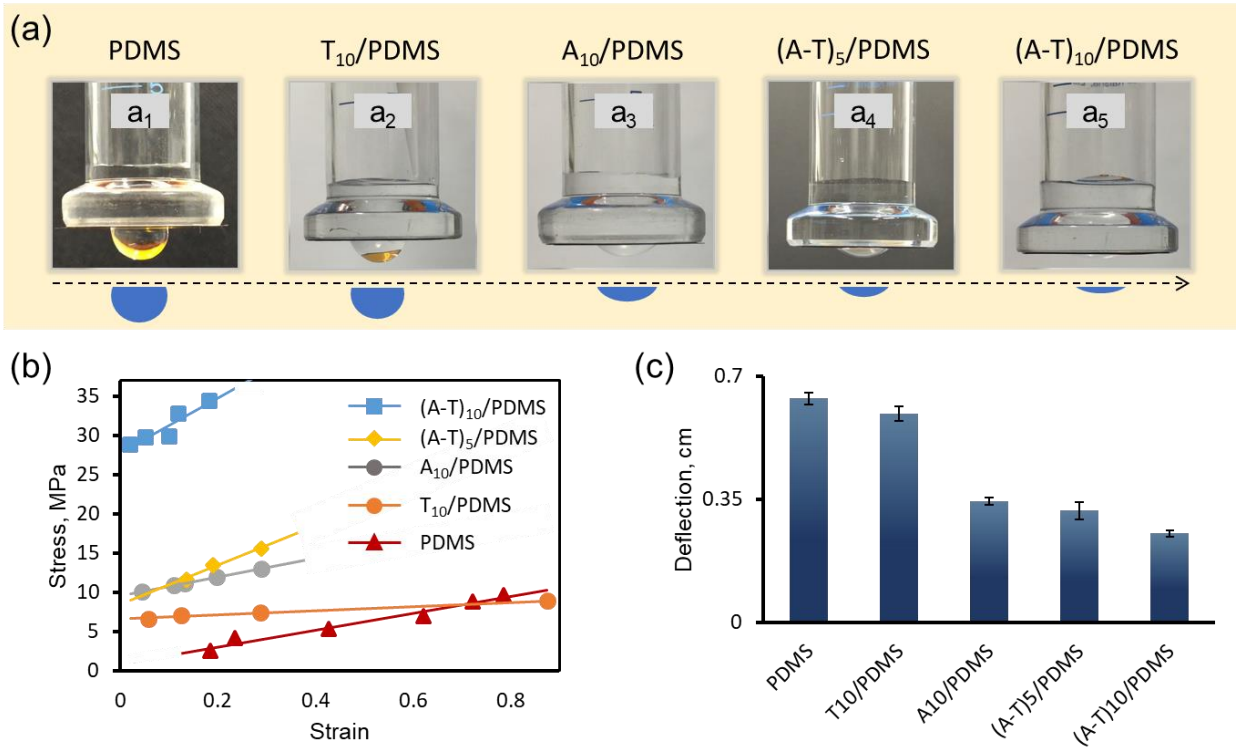

Figure 4-15. (a) Digital image showing deflection of different nanomembranes against an equal hydraulic pressure of 312.1 Pa. The blue semicircles below the images represent a clearer view of the bulges. (b) Tensile stress-strain plots of nanomembranes and their linear fits. (c) Maximum deflection at the corresponding rupture pressure.

The stress-strain curves showed linear relationship (Figure 4-15b). The maximum percent strain was 83.6% for PDMS, while the least was 18.2% for $(A\text{-}T)_{10}$/PDMS, signifying the contribution of crosslinked ASNTs on the dramatic increase in membrane stiffness. Yet, an 18.2% elongation in the case of $(A\text{-}T)_{10}$/PDMS indicated that the composite nanomembrane was flexible. The maximum membrane deflections before membrane breaking (Figure 4-15c) were also consistent with strain values.

To further characterize the mechanical robustness of the ASNTs-scaffolded PDMS nanomembrane, ultimate tensile strength and biaxial modulus were calculated and presented graphically in Figure 4-16. The ultimate tensile strength reflects the highest stress at the rupture point.

When comparing the tensile strength of nano-scale and bulk PDMS, the 90 nm-thick pristine PDMS (calculated to have 8.9 MPa) was slightly higher than that of bulk PDMS (7.1 MPa) reported elsewhere.[31] The difference in mechanical strength could be due to rearrangement of the

polymer chains during stretching in the nanothick PDMS film, which is relatively less probable in the bulk PDMS. Bulk property (where material property is independent of its dimension) of PDMS is observed at thicknesses > 200 μm.[42]

On the other hand, the ASNT-scaffolded nanomembrane, $(A\text{-}T)_{10}$/PDMS, experienced high tensile strength of 34.6 MPa, which is approximately 4-times higher than that of pristine PDMS nanomembrane of comparable thickness. Similarly, the biaxial modulus of $(A\text{-}T)_{10}$/PDMS was 172 MPa, much larger than pristine PDMS (3.9 MPa). This dramatic improvement in tensile strength and biaxial modulus is indeed the result of the crosslinked nanofiber scaffolds. The one-dimensional structure of ASNTs and OH-functionalized surfaces[25] contribute for TiO_2-crosslinking and direct interactions among ASNTs themselves. These covalent and non-covalent interactions strengthen the network of ASNTs. Well-entangled and crosslinked network of ASNTs reinforced the strength of the overall nanomembrane.

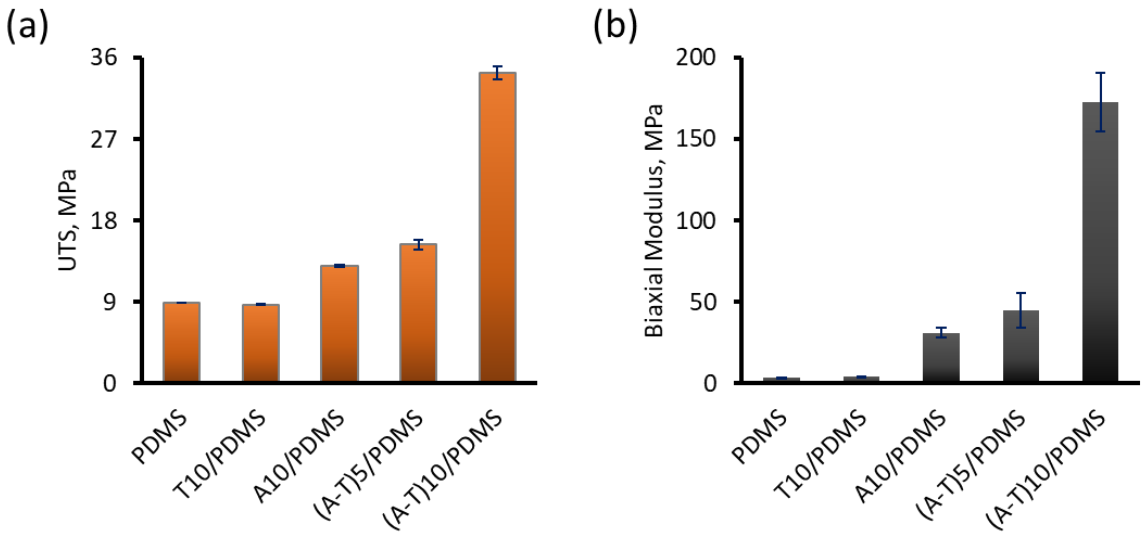

Figure 4-16. (a) The ultimate tensile strength (UTS) of nanomembranes determined from stress-strain curve. (b) The biaxial modulus of nanomembranes.

Again, the nanofiber scaffold was not too rigid (Figure 4-9a) due to the inherently flexible nature of the ASNTs so that the composite nanomembrane was quite flexible. In addition, when looking closely the interfacial structure of the nanofiber scaffold and PDMS, the polymer embedded into the rough nanotube network structure (Figure 4-8b,f). The partial embedment increases the polymer-scaffold interfacial area of binding,[43] contributing to the mechanical reinforcement of the whole composite nanomembrane.

In comparison to the known epoxy-resin based robust polymeric nanomembranes,[6,44] ASNT-scaffolded PDMS nanomembranes demonstrated higher mechanical toughness with more than double tensile strength, although the reported epoxy nanomembranes were thinner than the present nanomembrane. The flexibility of the present nanomembrane was also much higher (about two orders of magnitude) than the epoxy nanomembranes, clearly suggesting its robustness.

Table 4-3. Comparison of tensile strengths of the present nanomembranes with epoxy resin-based nanomembranes and bulk PDMS.

Membrane	Thickness	UTS (MPa)	Reference
PDMS (Bulk)	> 200 µm	7.1	[42]
PDMS (Nano-thick)	90 nm	8.9	Present work
$(A\text{-}T)_{10}$/PDMS	85 nm	34.6	Present work
PCGF/PEI/PLGA	70 nm	14.8-17.9	[6]
PCGF-PEI	24 nm	22.0	[6, 44]

4.3.4.3 Estimation of elastic modulus

A composite mechanical model has been employed to estimate the elastic modulus of $(A\text{-}T)_{10}$/PDMS composite nanomembrane. However, there is no suitable model that can be directly applied to the present nanotube-scaffolded polymer composite membrane structure, which is illustrated schematically in Figure 4-7. Available models assume that the nanofiber fillers are distributed throughout the polymer matrix, which is not the case in the current membrane. Thus, a modified Halpin-Tsai model[45,46] for composites reinforced by randomly oriented fibers[47,48] was employed. In selecting the model, the following assumptions were considered on the basis of the membrane structure.

- ASNTs are considered as randomly oriented fillers embedded in the PDMS matrix (based on the SEM image in Figure 4-8b).
- Even if ASNTs form bundles and are also cross-linked by TiO_2 that leads to continuous nanofibrous networks, the ASNTs are treated as independent fibers with identical size and shape.

For composites with aligned short fibers, the Halpin-Tsai model describes the elastic modulus as;

$$E_c = E_m\left(\frac{1+\zeta\eta V_f}{1-\zeta\eta V_f}\right) \quad \text{(Eq. 4-5)}$$

$$\eta = \frac{E_f/E_m - 1}{E_f/E_m + \zeta} \quad \text{(Eq. 4-6)}$$

where E_c, E_m and E_f are Young's modulus of the composite, matrix and fiber, respectively. V_f is volume fraction of the fiber.

And ζ is a parameter that depends on the geometry of the filler and takes the following forms. $\zeta = 2l/d$ for the determination of longitudinal modulus, and $\zeta = 2$ for the calculation of transversal modulus. *l* and *d* are the length and diameter of the nanotubes. In ASNT case, the values of *l* and *d* are considered as ~ 1 μm and 2.6 nm, respectively.

When the value of ζ becomes very small ($\zeta \rightarrow 0$), the Halpin-Tsai model reduces to the series model.

$$E_c = \frac{E_f E_m}{E_f V_m + E_m V_f} \quad \text{(Eq. 4-7)}$$

where V_m is volume fraction of the matrix.

When the value of ζ becomes very large ($\zeta \rightarrow \infty$), the Halpin-Tsai model reduces to the parallel model.

$$E_c = E_m V_m + E_f V_f \quad \text{(Eq. 4-8)}$$

For composites reinforced by randomly oriented fibers, the Halpin-Tsai equation could be modified as follows. This is the closest form of the Halpin-Tsai equation to determine the elastic modulus of the membrane structure in the present study.

$$E_c = E_m\left[\frac{3}{8}\left(\frac{1+\zeta\eta_L V_f}{1-\eta_L V_f}\right) + \frac{5}{8}\left(\frac{1+2\zeta\eta_T V_f}{1-\eta_T V_f}\right)\right. \quad \text{(Eq. 4-9)}$$

Where $\eta_L = \frac{E_f/E_m - 1}{E_f/E_m + 2l/d}$ (Eq. 4-10)

$$\eta_T = \frac{E_f/E_m - 1}{E_f/E_m + 2} \quad \text{(Eq. 4-11)}$$

$$\zeta = {}^{2l}/_{d} \qquad \text{(Eq. 4-12)}$$

In the case of ASNTs, the value of ζ is approximated as 770; i.e., ζ can neither be zero nor infinitive. Meaning that the reduced forms of the Halpin-Tsai model (Series and Parallel models) could not be applicable.[47] This supplements the above assumptions made based on the present membrane structure.

Thus, the modulus values are calculated using Eq. 4-9 and summarized in Table 4-4 under. Modulus values of 2.1 MPa[31] and 280 GPa[28] have been used for PDMS (matrix) and ASNTs (fiber), respectively. The volume fractions of the nanotubes and PDMS are estimated from the corresponding thicknesses of the whole composite nanomembrane (100 nm) and bare ASNT network (14 nm). Accordingly, $V_f \sim 0.14$ and $V_m \sim 0.86$. The elastic modulus estimated by series and parallel models are also presented in Table 4-4 for comparison.

Table 4-4. Elastic modulus calculated by Halpin-Tsai model and from biaxial modulus.

Method	Halpin-Tsai model, (Eq. 4-9)	Series model (Eq. 4-7)	Parallel model (Eq. 4-9)	From bulging data (Eq. 4-13)
Elastic modulus, MPa	100.82	2.44	39201.80	120.00

The elastic modulus (E) of $(A\text{-}T)_{10}$/PDMS and A_{10}/PDMS was also estimated from the experimental bulging data using biaxial modulus (Y) and Poisson's ratio (ν) as follows.[32] The result is listed in Table 4-4.

$$E = Y\,(1-\nu) \qquad \text{(Eq. 4-13)}$$

When comparing the elastic modulus obtained from model-based (~ 101 MPa) calculation and that determined from biaxial modulus, the results are more or less comparable. However, it is noteworthy that although the model-based calculations could not distinguish between $(A\text{-}T)_{10}$/PDMS and A_{10}/PDMS, the bulging-based elastic modulus of A_{10}/PDMS (21 MPa) and $(A\text{-}T)_{10}$/PDMS (120 MPa) values have big differences. This deviation should mainly be attributed to the crosslinking of nanofiber networks in the case of $(A\text{-}T)_{10}$/PDMS, which is not the case in A_{10}/PDMS.

4.3.4.4 LBL assembly of ASNT/PDMS as alternative approach

Finally, it is worth highlighting that PDMS/ASNT/PDMS sandwich structure and LBL deposition of ASNTs and PDMS (Figure 4-17c) was tested as an alternative route for preparing mechanically reinforced ASNT/PDMS composite nanomembrane.

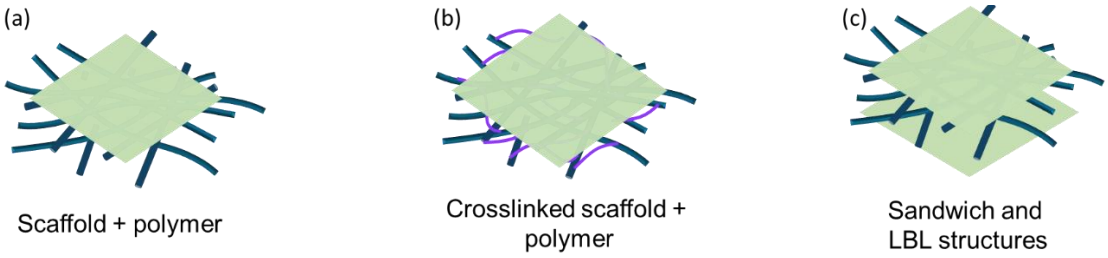

Figure 4-17. Schematic representation of nanofiber/polymer composite membrane preparation approaches. (a) Polymer deposited on pre-coated bare ASNT scaffold. (b) Polymer deposited on crosslinked ASNT scaffold. Structures (a) and (b) are simply the schematics of A_{10}/PDMS and (A-T)10/PDMS membranes respectively, which are discussed in previous sections. These diagrams are shown here for easy comparison.

However, this approach had some limitations like (i) surface activation of PDMS is required to deposit ASNTs on the surface of PDMS. Unfortunately, the O_2 plasma treatment damages the PDMS nano-layer (even at very short exposure, say 2 seconds, Figure 4-18), making it difficult to make defect-less nanomembrane. (ii) The membrane preparation process is technically inadequate and time consuming, especially in the case of LBL assembly as repeated O_2 plasma activation is needed after each PDMS coating. (iii) Above all, there was no gain from the viewpoint of mechanical property improvement.

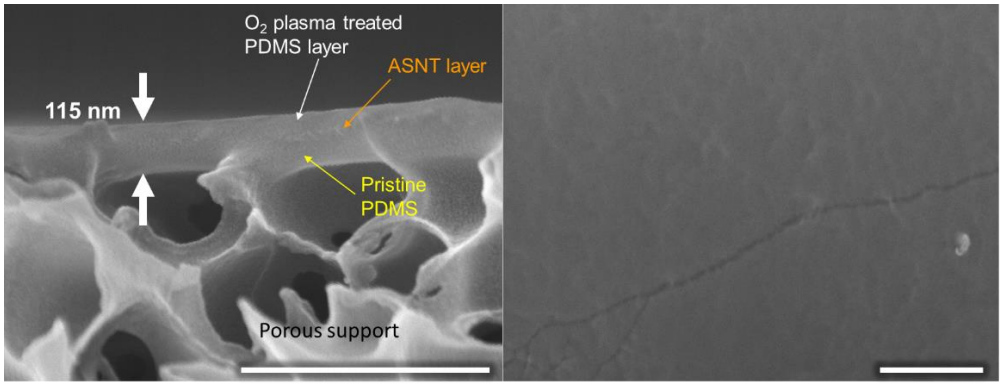

Figure 4-18. Cross-sectional structure (a) and surface morphology (b) of PDMS/ASNT/PDMS sandwich nanomembrane. The membrane was inverted up-side-down during transfer onto porous support – to observe the O_2 plasma treated PDMS side. **Scale bar: 500 nm**.

4.3.5 Gas separation property

Since one of the challenges in the development of FS-NMs is the difficulty to avoid pinhole formation, gas separation experiment was conducted in order to confirm the absence of defects in the nanomembranes. The detailed gas permeation measurement procedure was described elsewhere,[10] and discussed in Chapter 2. A 50:50 mixture of CO_2 and N_2 was used as a feed gas. The $(A\text{-}T)_{10}$/PDMS nanomembrane could hold a feed pressure of up to 0.2 MPa. The CO_2/N_2 selectivity was about 7, and permeance of CO_2 was 109 GPU (1 GPU: 7.5×10^{-12} $m^3/m^2\cdot s\cdot Pa$, at standard temperature and pressure), Figure 4-19. The pressure holding capacity and selective gas separation of CO_2 over N_2 implied that the ASNT-scaffolded composite nanomembrane was defectless. The preferential CO_2 permeation over N_2 is mainly ascribed to the PDMS layer.[49] And, in fact, the CO_2/N_2 selectivity of thick PDMS membrane, is known to be about 11, which is slightly higher than that of $(A\text{-}T)_{10}$/PDMS membrane. Yet, the observed CO_2/N_2 selectivity of $(A\text{-}T)_{10}$/PDMS membrane confirms that the nanomembrane does not have serious defects that can lead to simple gas leak without any selectivity. The unexpected low permeance of $(A\text{-}T)_{10}$/PDMS compared to pristine PDMS may be due to the presence of amorphous TiO_2, which was used as a crosslinker for ASNTs.

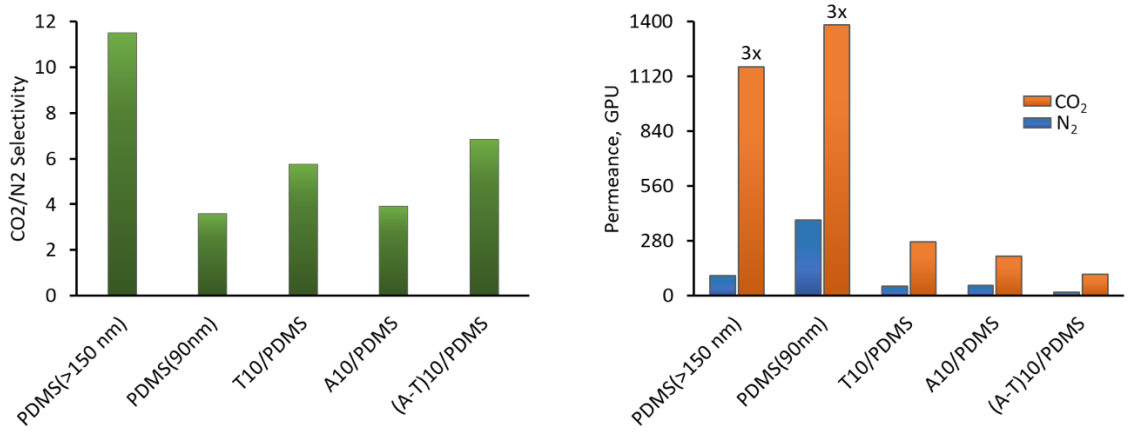

Figure 4-19. CO_2/N_2 selectivity (left) and permeance of CO_2 and N_2 (right) of various nanomembranes. PDMS with 90 nm thickness has lower CO_2/N_2 selectivity than the thicker counterparts; could be associated to the formation inclusion of pin-holes upon membrane thinning.

4.4 Discussion

The key factor behind the developed tough, flexible and free-standing nanomembrane is the incorporation of very thin (~15 nm) ASNTs backbone structure (Figure 4-20a). The volume or thickness contribution of the ASNT scaffold layer is less than 15% of the whole composite nanomembrane. However, this ultrathin network structure brought about dramatic enhancement on the mechanical property of the PDMS nanofilm.

The structural function of the aluminosilicate nanotube scaffold in my membrane design resembles that of the cytoskeleton in biological membranes.[50] As depicted in Figure 4-20b, the cytoskeleton is the "frame" of the cell, keeping structures in place, providing support, and giving the cell a definite shape. The cytoskeletal microtubules and filaments have crosslinkers to control the structural organization of their networks. Likewise, the TiO_2 in $(A\text{-}T)_n$/PDMS nanomembranes plays crosslink and strengthen the ASNT networks. When shear stresses are applied to the cell, such cytoskeletal networks stiffen and resist additional deformation. They are also elastic enough to undergo softening after compressive stress. Similarly, the ASNT networks scaffold the elastomeric PDMS and restrict its deformation during mechanical stress, while experiencing stretching upon a progressive increase in mechanical load. The elongation of the ASNT scaffolds along with the polymer networks could be due to disassembling of the ASNT network structure, which allows rearrangement and alignment of the fiber structures in the direction of tensile stretching.

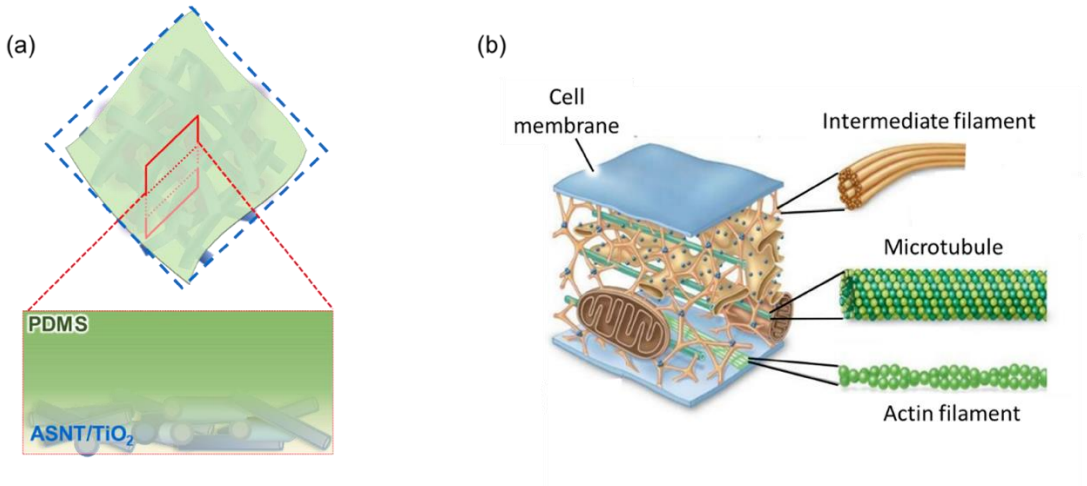

Figure 4-20. Schematic illustration of ASNT-scaffolded PDMS nanomembrane (a) and cytoskeleton (b). Diagram 'b' source: https://crossfithartford.com.

4.5 Conclusion

In summary, mechanically strong, flexible, free-standing and sub-100 nm thick nanofiber-scaffolded polymer nanomembrane has been developed. The incorporation of cytoskeleton-inspired ASNT networks presented remarkable enhancement in the tensile strength and biaxial modulus of the polymer nanomembrane, while maintaining flexibility in the composite nanomembrane. Such biomimetic strategy can be extended to the development of other mechanically strong FS-NMs of diverse polymer materials, including polymers of less-film-forming nature. Other fibrous materials such as cellulose nanofiber could also be utilized as an alternative to ASNTs.

References

(1) Rogers, J. A.; Lagally, M. G.; Nuzzo, R. G. *Nature* **2011**, *477* (7362), 45–53.

(2) Li, Z.; Ma, G.; Ge, R.; Qin, F.; Dong, X.; Meng, W.; Liu, T.; Tong, J.; Jiang, F.; Zhou, Y. *Angew. Chem. Int. Ed.* **2016**, *55* (3), 979–982.

(3) Meyerbröker, N.; Zharnikov, M. *Adv. Mater.* **2014**, *26* (20), 3328–3332.

(4) Fujie, T. *Polym. J.* **2016**, *48* (7), 773–780.

(5) Fujikawa, S.; Muto, E.; Kunitake, T. *Langmuir* **2009**, *25* (19), 11563–11568.

(6) Schuster, C.; Rodler, A.; Tscheliessnig, R.; Jungbauer, *Sci. Rep.* **2018**, *8* (1), 4410.

(7) Watanabe, H.; Vendamme, R.; Kunitake, T. *Bull. Chem. Soc. Jpn.* **2007**, *80* (3), 433–440.

(8) Cheng, W.; Campolongo, M. J.; Tan, S. J.; Luo, D. *Nano Today* **2009**, *4* (6), 482–493.

(9) Huang, G.; Mei, Y. *Adv. Mater.* **2012**, *24* (19), 2517–2546.

(10) Mersha, A.; Selyanchyn, R.; Fujikawa, S. *CleanE* **2017**, *1* (1), 80–89.

(11) Shi, Y.; Peng, L.; Ding, Y.; Zhao, Y.; Yu, G. *Chem. Soc. Rev.* **2015**, *44* (19), 6684–6696.

(12) Dong, G.; Li, H.; Chen, V. *J. Mater. Chem. A* **2013**, *1* (15), 4610.

(13) Zhu, X.; Tian, C.; Do-Thanh, C. L.; Dai, S. *ChemSusChem* **2017**, *10* (17), 3304–3316.

(14) Rajan, G. S.; Sur, G. I. L. S.; Mark, J. E.; Schaefer, D. W.; Beaucage, G. *J. Polym. Sci. Part B Polym. Phys.* **2003**, *41*, 1897–1901.

(15) Vendamme, R.; Onoue, S.-Y.; Nakao, A.; Kunitake, T. *Nat. Mater.* **2006**, *5* (6), 494–501.

(16) Ye, Y. N.; Frauenlob, M.; Wang, L.; Tsuda, M.; Sun, T. L.; Cui, K.; Takahashi, R.; Zhang, H. J.; Nakajima, T.; Nonoyama, T. *Adv. Funct. Mater.* **2018**, *28* (31), 1801489.

(17) Richardson, J. J.; Bjornmalm, M.; Caruso, F. *Science* **2015**, *348* (6233), 2491.

(18) Jimenez-Solomon, M. F.; Gorgojo, P.; Munoz-Ibanez, M.; Livingston, A. G. *J. Memb. Sci.* **2013**, *448*, 102–113.

(19) Droudian, A.; Youn, S. K.; Wehner, L. A.; Wyss, R. M.; Li, M.; Park, H. G. *ACS Appl. Mater. Interfaces* **2018**, *10* (23), 19305–19310.

(20) Sorribas, S.; Gorgojo, P.; Téllez, C.; Coronas, J.; Livingston, A. G. *J. Am. Chem. Soc.* **2013**, *135* (40), 15201–15208.

(21) Yoshinaga, N.; Aomine, S. *Soil Sci. Plant Nutr.* **1962**, *8* (3), 22–29.

(22) Cradwick, P. D. G.; Farmer, V. C.; Russell, J. D.; Masson, C. R.; Wada, K.; Yoshinaga, N. *Nat. Phys. Sci.* **1972**, *240* (104), 187–189.

(23) Ma, W.; Yah, W. O.; Otsuka, H.; Takahara, A. *J. Mater. Chem.* **2012**, *22* (24), 11887–

11892.

(24) Ichinose, I.; Senzu, H.; Kunitake, T. *Chem. Mater.* **1997**, *9* (6), 1296–1298.

(25) Kang, D.-Y.; Brunelli, N. A.; Yucelen, G. I.; Venkatasubramanian, A.; Zang, J.; Leisen, J.; Hesketh, P. J.; Jones, C. W.; Nair, S. *Nat. Commun.* **2014**, *5* (1), 3342.

(26) Majumder, M.; Chopra, N.; Hinds, B. J. *ACS Nano* **2011**, *5* (5), 3867–3877.

(27) Wu, Z. *Science* **2004**, *305* (5688), 1273–1276.

(28) Guimarães, L.; Enyashin, A. N.; Frenzel, J.; Heine, T.; Duarte, H. A.; Seifert, G. *ACS Nano* **2007**, *1* (4), 362–368.

(29) Lu, J. P. *Phys. Rev. Lett.* **1997**, *79* (7), 1297–1300.

(30) Farmer, V. C. *Clay Miner.* **1983**, *18* (4), 459–472.

(31) Johnston, I. D.; McCluskey, D. K.; Tan, C. K. L.; Tracey, M. C. *J. Micromech. Microeng.* **2014**, *24* (3), 035017.

(32) Small, M. K.; Nix, W. D. *J. Mater. Res.* **2011**, *7*, 1553–1563.

(33) Kojio, K.; Nagano, C.; Fujimoto, A.; Nozaki, S.; Yokomachi, K.; Kamitani, K.; Watanabe, H.; Takahara, A. *Soft Matter* **2018**, *14* (9), 1659–1664.

(34) Lee, J. N.; Park, C.; Whitesides, G. M. *Anal. Chem.* **2003**, *75* (23), 6544–6554.

(35) Mukherjee, S.; Kim, K.; Nair, S. *J. Am. Chem. Soc.* **2007**, *129* (21), 6820–6826.

(36) Mukherjee, S.; Bartlow, V. M.; Nair, S. *Chem. Mater.* **2005**, *17* (20), 4900–4909.

(37) Ibach, H. *J. Chem. Inf. Model.* **2013**, *53* (9), 1689–1699.

(38) Shircliff, R. A.; Stradins, P.; Moutinho, H.; Fennell, J.; Ghirardi, M. L.; Cowley, S. W.; Branz, H. M.; Martin, I. T. *Langmuir* **2013**, *29* (12), 4057–4067.

(39) O'Hare, L. A.; Hynes, A.; Alexander, M. R. *Surf. Interface Anal.* **2007**, *39*, 926–936.

(40) Kang, E.; Ryoo, J.; Jeong, G. S.; Choi, Y. Y.; Jeong, S. M.; Ju, J.; Chung, S.; Takayama, S.; Lee, S. H. *Adv. Mater.* **2013**, *25* (15), 2167–2173.

(41) Das, M.; MacKintosh, F. C. *Phys. Rev. Lett.* **2010**, *105* (13), 1–4.

(42) Liu, M.; Sun, J.; Sun, Y.; Bock, C.; Chen, Q. *J. Micromech. Microeng.* **2009**, *19* (3), 035028.

(43) Gan, Y. X. *Int. J. Mol. Sci.* **2009**, *10* (12), 5115–5134.

(44) Watanabe, H.; Kunitake, T. *Adv. Mater.* **2007**, *19* (7), 909–912.

(45) Halpin, J. C. *J. Compos. Mater.* **1969**, *3* (4), 732–734.

(46) Patterson, W.; Force, A. *Polymer Engineering and Science* **1976**, *16* (5), 344-352.

(47) Loos M. Fundamentals of polymer matrix composites containing CNTs. In *Carbon Nanotube Reinforced Composites*; Elsevier: Amsterdam, The Netherlands, **2015**; pp. 125–170.

(48) Tucker, C. L.; Liang, E. *Compos. Sci. Technol.* **1999**, *59* (5), 655-671.

(49) Robb, W. L. *Ann. N. Y. Acad. Sci.* **1968**, *146*, 119–137.

(50) Fletcher, D. A.; Mullins, R. D. *Nature* **2010**, *463* (7280), 485–492.

Chapter 5 Summary and outlook

The thesis presented a significant step-forward study in addressing the challenges of developing mechanically robust functional FS-NMs. Basically, organic/inorganic composites are employed as membrane materials to take advantage of the flexibility of polymers and rigidity of inorganics.

Initially, a surface sol-gel induced LBL assembly of metal oxides and polymers as well as blend type approaches were investigated. The challenges encountered in the path were addressed by changing membrane materials and structural design. Ultimately, a unique strategy has been developed for the preparation of free-standing and mechanically tough, yet functional polymeric nanomembranes. The method involves the incorporation of crosslinked aluminosilicate nanotube networks as a bed scaffold in order to anchor and strengthen polymeric nanofilms. Here, the key achievement is the development of crosslinked nanofibrous scaffold that brought about dramatic mechanical reinforcement to polymeric nanomembranes of sub-100 nm thickness. The presented unconventional approach could be extended to various polymeric materials (including polymers of less film-forming nature) as a general route to fabricate strong FS-NMs for broad-spectrum of applications such as sensing devices, energy conversion and storage, wound dressing, as well as cellular and nanoparticle organization.

To realize the potential of the presented research achievements (specifically, ASNT-scaffolding approach) in overcoming the barriers of FS-NMs for practical applications, it is worth identifying experimental gaps and key directions for future investigations.

- To understand the mechanism of mechanical reinforcement in more detail, modeling the relationship between the presented nanomembrane structure and its mechanical property would be helpful.
- In addition, further investigation of the interfacial interactions as well as degree of polymer interpenetration into the nanotube scaffold would open up opportunities to fine tune polymer-scaffold interactions and consequent mechanical properties.
- To enhance the efficiency of these nanotube-scaffolded composite nanomembranes for applications such as separation, solid electrolytes and sensing, it is essential to consider crosslinkers that are task-specific to the desired purpose so that the interspace in the network structure could be utilized.

- Assuming the utilization of suitable crosslinker (as described above), it would be possible to access the inner pores of the ASNTs. However, the accessible pores might be limited due to shielding from crosslinker and polymer-top-layer,as well as bundling.
- Internal and external surface functionalization of the ASNTs.[1–3] prior to membrane preparation would assist in controlling the interaction with polymers, as well as in tailoring the properties and function of the resulting composite FS-NMs.

References

(1) Ma, W.; Yah, W. O.; Otsuka, H.; Takahara, A. *Beilstein J. Nanotechnol.* **2012**, *3* (1), 82–100.

(2) Zanzottera, C.; Vicente, A.; Celasco, E.; Fernandez, C.; Garrone, E.; Bonelli, B. *J. Phys. Chem. C* **2012**, *116* (13), 7499–7506.

(3) Kang, D.-Y.; Brunelli, N. A.; Yucelen, G. I.; Venkatasubramanian, A.; Zang, J.; Leisen, J.; Hesketh, P. J.; Jones, C. W.; Nair, S. *Nat. Commun.* **2014**, *5* (1), 3342.

Acknowledgement

First and foremost, I am grateful to the blessings from God Almighty for giving me the strength and inspiration to undertake this research study and accomplish successfully.

I would also like to express my gratitude to my supervisor Assoc. Prof. Shigenori Fujikawa for his support, guidance and inspiration. This research journey with him made a difference in my life one way or another.

My gratitude also goes to Prof. Atsushi Takahara and Prof. Noriho Kamiya. Their guidance, as well as time and effort in reviewing my dissertation is well appreciated.

I am also indebted to the Japanese Government, Ministry of Education, Culture, Sports, Science and Technology (MEXT) for funding my Ph.D. study.

My sincere thanks are also due to Prof. Sheng Dai (Oak Ridge National Laboratory and the University of Tennessee, USA) for giving me the visiting research opportunity in his laboratory at the Joint Institute of Advanced Materials (JIAM, UT-ORNL), September 2018 – November 2018. His support and encouragement is well appreciated.

I am grateful to Prof. Naotoshi Nakashima for his inspiration, valuable discussion and carrier advice. It is also a pleasure to acknowledge the fruitful discussions and directions from Prof. Sandra Kentish. I would like to thank my laboratory members Ms. Miho Ariyoshi and dr. Roman Selyanchyn for their support during my research study.

Last but not least, I would like to express my warmest gratitude to my family for their unreserved support and encouragement. They have been the source of my courage and inspiration throughout my study years. Thanks are also due to my friends who have been of any support for the successful accomplishment of my doctoral study.

Anteneh Mersha

Department of Chemistry and Biochemistry

Graduate School of Engineering

Kyushu University, Fukuoka, Japan

March 2019